# Analytical and Experimental Evaluation of Multivariable Stability Margins

John K. Berg

A thesis
submitted in partial fulfillment of the
requirements for the degree of

Master of Science in Aeronautics and Astronautics

University of Washington

2020

Reading Committee:

Kristi Morgansen

Eli Livne

Program Authorized to Offer Degree:
Aeronautics and Astronautics

University of Washington

## Abstract

Analytical and Experimental Evaluation of Multivariable Stability Margins

John K. Berg

Chair of the Supervisory Committee:
Professor Kristi Morgansen
Department of Aeronautics and Astronautics

This work addresses control law synthesis for active flutter suppression followed by the design and development of an active flexible wind tunnel model representative of high aspect ratio commercial aircraft. An initial early-design math model of the structural dynamics, unsteady aerodynamics, sensing, and actuation of the system was used to synthesize three control laws that would stabilize the system against flutter over a range of speeds below and above the passive open-loop flutter speed. Three methods for establishing closed-loop robustness measures were used to quantify the robustness of the system based on its initial mathematical model. The system was then tested with these control laws, and their robustness to system variations in the wind tunnel was studied. Such variations included speed as well as gain and phase in the control loops, representing gain and phase uncertainties in the system. This was followed by revisiting the robustness of the control laws with mathematical testing, this time with a more accurate mathematical model of the system. The work adds insight regarding the kind of model variations that the control designer needs to consider and the way different measures of system robustness compare to one another and relate to the capacity of the control design to permit model uncertainties.

# TABLE OF CONTENTS

# LIST OF FIGURES

# LIST OF TABLES

# ACKNOWLEDGMENTS

I would like to first thank my advisors Professor Kristi Morgansen and Professor Eli Livne. Thank you Kristi for the guidance you've given me and patience you've shown towards me over these past several years. Thank you Eli for the late-night discussions and for the enthusiasm that you've given me for the topics I now study. I also owe thanks to all the members of the Nonlinear Dynamics and Control Lab who have assisted me over the years.

I would also like to thank Professor Sergio Ricci and his team at the Polytechnic of Milan; their work helped create the experimental results seen in this thesis.

# DEDICATION

For my wife Becky and children, Jenson and Lucy.

# Chapter 1

# INTRODUCTION

Renewed interest in active flutter suppression has led to rising efforts in recent years to revisit it, evaluate it, and build more experience with this technology. These efforts are driven partly by recent developments in instrumentation, sensing, control theory, and hardware, and partly by the emergence of novel unconventional flight vehicle configurations for which the prevention of aeroelastic and aeroservoelastic dynamic instabilities with passive airframe solutions may be too costly or too impractical. A comprehensive review of the history and state of the art of active flutter suppression (AFS) can be found in [1]. Recent AFS research using UAVs especially designed for the task is described in [2–6]. But with more than 50 years of AFS history, the technology is still not considered ready for wide scale implementation.

From the design perspective, the tradeoff outcomes are not clear once reliability, maintainability, and safety constraints are accounted for. To meet such constraints, the weight, cost, and complexity of AFS systems may end up higher than those of passive solutions. Moreover, the questions and challenges of how to approach the safety issue – how to consider AFS safety from the early stages of the design process, how to evaluate safety, how to design for safety, and how to demonstrate safety in a way that would meet certification requirements – and the research that they inspire are still evolving.

From a control technology perspective, the issues of control system synthesis for robustness and closed-loop dynamic systems robustness evaluation have been pursued for years [7–11], leading to a vast body of experience and literature. The AFS challenge is unique and quite challenging, however. The physics of the flutter problem is often difficult to capture accurately by analysis. Both wind tunnel tests and flight tests can be expensive, complex, and risky. The problem is multi-

disciplinary in nature, and the interdisciplinary interactions involved can be difficult to understand, often with nasty surprises in the form of hardware failures that were neither expected nor well-predicted when they were expected.

This paper presents some recent results of a collaborative research effort by the Polytechnic of Milan, Italy, (POLIMI) and the University of Washington (UW) in Seattle to gain experience with and new insights into AFS technology, with a focus on the AFS synthesis and implementation processes, the performance of alternative control law synthesis strategies, the uncertainties involved in each step of the development, the robustness of resulting control systems as determined by analysis, and the robustness of those systems as measured in AFS wind tunnel tests [12].

A companion paper [13] presents the development of the wind tunnel model, the wind tunnel testing capabilities, test procedures, and the process of building mathematical models of the system (and the uncertainty analysis and test evaluation involved). The present paper focuses on control law synthesis, control law performance evaluation by analysis, and control law performance in tests in the face of flight conditions and dynamic system uncertainties. In particular a focus was placed on three control law synthesis techniques: the ILAF method (Identical Locations of Accelerations and Forces) [14–17], LQG/LQR, and Static Output Feedback (SOF) [18–20]. The present paper and its companion paper will serve as the foundation for future research carried out using the new model and AFS testing capabilities at POLIMI.

The paper begins in chapter 2 with a brief presentation of the aeroservoelastic wind tunnel system developed for this research. The synthesis of the control laws studied, the ILAF, LQR/LQG, and SOF laws, is presented next (chapters 3 and 4), together with analytical evaluation of their robustness properties (chapter 5). Selected wind tunnel test results follow in chapter 6, including time response histories of the system in open-loop and closed-loop conditions, and stability boundaries measured as functions of variations in speed, control system gains, and control system delays. Correlations between wind-tunnel tests and the analyses using the multi-loop stability margins and perturbed root loci are conducted in chapter 7 and major lessons and recommendations for future work are provided in chapter 8.

# Chapter 2

# AEROELASTIC MODEL

The aeroservoelastic wind tunnel experimental model developed for the active flutter suppression (AFS) studies presented here has been described in [12] and is shown in Figs. 1 and 2. For the AFS tests described in this paper, two ailerons were used, one on each wing, and "flutter Stopper" pods were attached to the wing tips. A moving mass in each of the wingtip pods could change location rapidly from a rear location, for which the passive (open-loop) speed of the model was well within the wind tunnel speed capabilities, to a forward location, for which the model was flutter-safe in the wind tunnel. When wing-tip acceleration reached a preset level, the flutter stoppers were activated, and the configuration changed abruptly to a stable configuration. Emphasizing versatility and flexibility in changing control laws from one set to another, tests using different control law strategies, or different variations of control laws in parametric studies could be carried out quickly and efficiently. If instability was encountered, the model was protected by the flutter stoppers, and resetting the model for the next run could be done very quickly. A system identification process using the same ailerons that were used for flutter suppression was run continuously during the tests. This feature of the wind tunnel model and its capabilities was important since using the same control surfaces for different functions, making sure that they did not saturate, and that no function was impaired is one of the challenges in optimizing actively-controlled airplanes.

The critical flutter mechanism of the model was symmetric. First steps in the development of mathematical models for the system are described in [12]. Additional work done during the program, as more test results became available, to identify sources of test / analysis discrepancy and improve the math models is described in the companion paper [13]. It is of interest to note that control laws tested during the tests presented in this paper were based on a mathematical model that did not capture the physics of the system as well as more recent mathematical models

which were developed based on accumulated test results. That is, in a way that is typical of the aircraft development process, much of the early control law synthesis and implementation work described here was based on a mathematical model whose flutter speed deviated from the flutter speed measured by tests. Discussion of this aspect of the control of the uncertain systems studied here will be presented in subsequent chapters of this paper.

The aeroservoelastic mathematical model of the wind tunnel experimental model includes its structural dynamics and unsteady aerodynamics as well as transfer functions of the 15 Hz actuators. The experimental model was supported on a system of flexible suspension springs with resulting rigid body natural frequencies that were low enough relative to the range of aeroelastic frequencies of aeroservoelastic "action" to render the model practically free-free. Doublet Lattice aerodynamics without correction factors were used first. The importance of aerodynamic correction factors when linear unsteady aerodynamic models are used is discussed in [21–24] and will be addressed later in the paper. The need to add high-pass and low-pass filters in the mathematical models used for simulation was recognized in order to filter out the effects of very low frequencies of the model on the cable system (knowing that they had no effect on the critical flutter mechanism) and to reflect the low-pass nature of the actuators (which beyond a certain high frequency become ineffective). The approximate sensor locations are shown in Fig. 2.1. Note that many more accelerometers are installed on the model than those used for the active flutter suppression control systems considered in this work. The flexible support cables can be seen in Fig. 2.2. Changes in wind tunnel dynamic pressure, location of flutter-stopper tip masses, and any structural dynamic or aerodynamic property (such as changes in aerodynamic correction factors that would better match linear aerodynamic theory to experiments) lead to variation in the state-space model matrices. With the simulation capabilities used for this work, state space models corresponding to variations in the physical properties of the wind tunnel system could be quickly generated.

Figure 2.3 shows a root locus of the passive (active control off) wind tunnel model system over a range of speeds from 15 m/s (green) to 60 m/s (red). Figure 2.3b shows the first wing-bending mode crossing the imaginary axis at approximately 41.5 m/s. Also visible in Fig. 2.3b is a structural mode at around 7.6 rad/s. Though not clear from the figure, this mode also moves

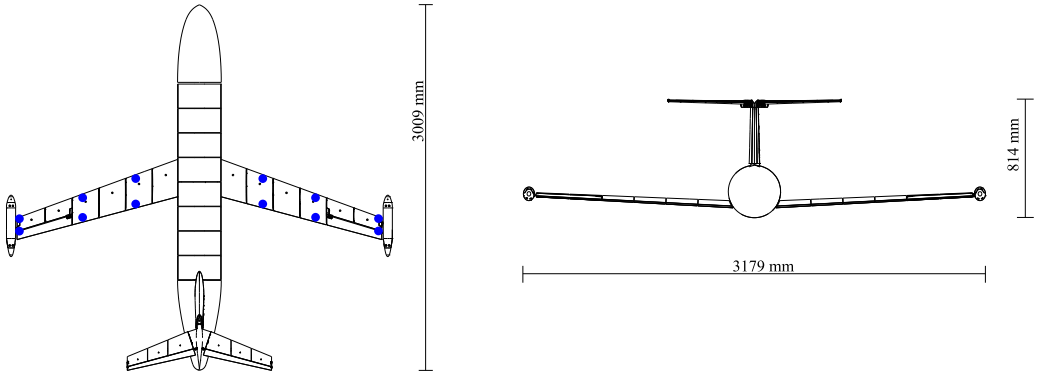


Figure 2.1: Dimensions of the active aeroelastic wind tunnel model. Approximate accelerometer locations are shown in blue.

towards the right half plane. Note that the analytical model without low and high pass filters that eliminate dynamic response in frequency regions in which the math model is inaccurate has three lightly damped modes, one at 7.6 rad/s and two at approximately 387 rad/s, that are not seen in the physical hardware. This original state space model inaccuracy is due to the high-reduced-frequency limit of the rational function unsteady aerodynamic matching and the aerodynamic inaccuracies at very low frequencies, where fore-aft rigid body motions need special modeling as well the extreme sensitivity of the accuracy of the unsteady aerodynamic matching to the derivative of the force coefficients with respect to reduced frequency around k=0. The low-pass and high-pass filters incorporated into the math model took care of the low-damped poles in the frequency regions that were of no interest in this study. The passive open-loop root locus results presented here do not account for any aerodynamic correction factors. Those were added later.

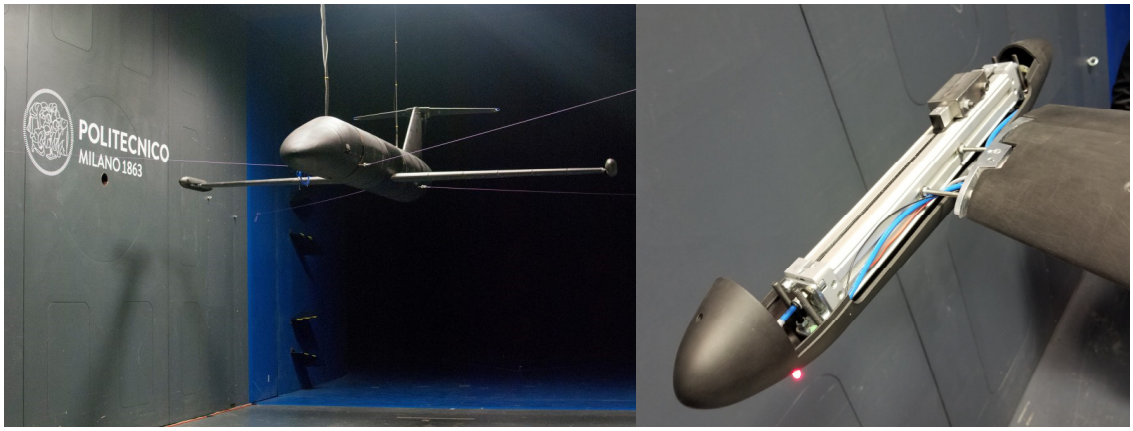


Figure 2.2: The active aeroelastic wind tunnel model installed in the POLIMI wind tunnel (left) and wing-tip flutter stoppers (right).

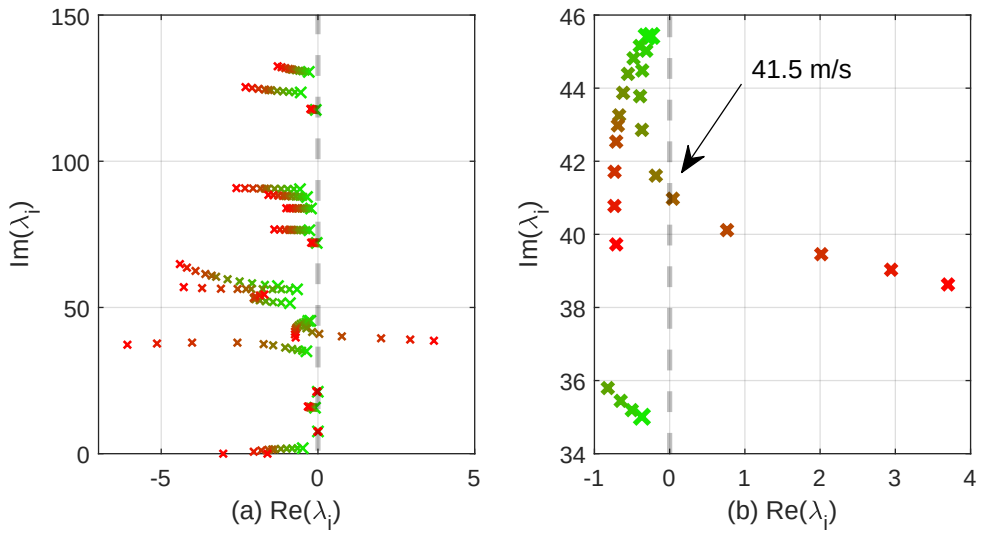


Figure 2.3: (a) Root locus for air-speeds from 15 m/s to 60 m/s. (b) Enlarged view of the first-wing bending pole crossing into the right half plane at 41.5 m/s.

# Chapter 3

# A BRIEF REVIEW OF SOME MULTIVARIABLE STABILITY MARGINS

The extension of the commonly used robustness estimation methods developed for Single Input Single Output (SISO) systems to the Multi-Input Multi-Output case (MIMO) case has not been straightforward. In what is now a classic example, work in [25] showed that a multivariable system can have excellent one-loop-at-a-time margins while having arbitrarily small margins to simultaneous perturbations in each loop. Despite the extensive research into MIMO stability robustness, the SISO-based loop-at-a-time margins continue to be used often by the practicing engineer and are, in fact, even written as requirements for the certification of flight control systems. Considering that active flutter suppression is not yet certified in general for commercial aviation [1], a renewed interest in and evaluation of multivariable stability margins was at the heart of the work presented here. Although quite a number of stability robustness evaluation methods for MIMO systems have been developed [26], the stability robustness analyses presented here will consider only two as a first step: the universal gain margin method [10] and the disk margin method [27]. Both resemble in engineering intuition the classical SISO gain and phase margin approaches and may be faster for the practicing aerospace control community to adopt although, of course, in any robustness evaluation of AFS control laws all leading methods of robustness analysis should be used and the tradeoffs, regarding performance versus conservatism in the design, should be carefully checked. The standard one-loop-at-a-time stability margins, the SISO margins are calculated one-loop-at-a-time, are also evaluated and compared against the multi-loop methods.

## *3.1 Disk Margin Analysis*

The disk margin analysis method was created first in [27], and has become a staple of modern stability analyses, possibly due to the ease-of-use in commercial software packages. The disk

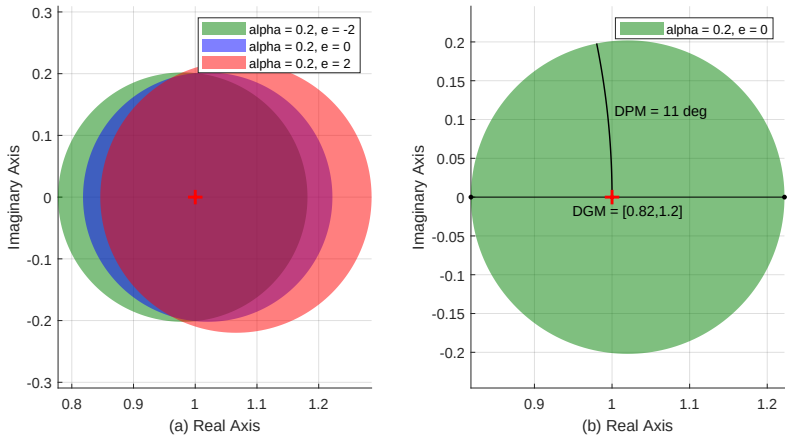


Figure 3.1: Figure (a): Skewing complex disk using eccentricity $e$. Figure (b): Disk-based gain margins and phase margins.

margin method involves finding the largest disk-shaped complex perturbation, $f$, typically placed at the plant input or output, that the system can tolerate before becoming unstable. The perturbation, $f$, is parameterized as

$$f = \frac{1 + \alpha\left(\frac{1-e}{2}\right)\delta}{1 - \alpha\left(\frac{1+e}{2}\right)\delta}, \quad \delta \in \mathbb{C}, \quad |\delta| < 1, \tag{3.1}$$

where $e$ is termed the eccentricity, and $\alpha$ conveys the disk size. The eccentricity, $e$, is the user-defined value that skews the complex disk away from the nominal value of 1. The power of the eccentricity parameter is in this ability to skew towards more or less gain, as shown in Fig. 3.1a. This feature is useful when knowledge of the likely changes in gain is given. However, in most cases the balanced disk margin, $e = 0$, is the preferred option [27]. For the MIMO analyses presented here, the complex perturbation is stacked into a diagonal matrix $F = \text{diag}(f_1, \ldots, f_n)$, and the stability analyses follow by placing the matrix $F$ at the input or output of the plant and finding the minimum destabilizing perturbation. As the complex perturbation is a disk, classical gain and phase margins can be found as shown in Fig. 3.1b.

The classical gain margins and phase margins shown in Figure 3.1b could also be used to

calculate margins for simultaneous changes in gain and phase since the interpretation of Fig. 3.1b is that the system is guaranteed stable for any perturbation within the disk. It is important to point out that, although the disk margin can be used for both single loop systems and multiple loop systems, the results presented here will consider only the multi-loop disk margin. Also worthy of noting is that the disk margin can easily accommodate analyses at the input and output simultaneously as the DM, for the MIMO case, is based upon the $M-\Delta$ framework of representing uncertainty. For more information on disk margin analysis, including SISO systems, and simultaneous perturbations at the input and output, the reader is referred to [28].

### *3.2 Universal Gain and Phase Margin*

The universal gain and phase margin method (UGM) is another method for estimating robustness of MIMO systems. It was created to establish universal gain and phase margins for MIMO systems as an extension of the margins that are used for SISO systems [10, 11]. The method is based on the minimum singular value of the return difference matrix (RDM) over a range of frequencies and has been used to evaluate and to synthesize many control laws in aeroservoelastic and flight control applications at NASA.

For an uncertain matrix, $L$, placed at the input or output of the MIMO plant, the perturbed system is stable if

$$\overline{\sigma}(L^{-1} - I) < \underline{\sigma}(I + GK), \tag{3.2}$$

where $\overline{\sigma}$ denotes the largest singular value and $\underline{\sigma}$ the smallest singular value. Eq. (3.2) is valid for any stable $L$. However, if $L = \text{diag}(k_1 e^{j\theta_1}, k_2 e^{j\theta_2}, \ldots, k_n e^{j\theta_n})$, then

$$\overline{\sigma}(L^{-1} - I) = \max \sqrt{\left(1 - \frac{1}{k_i}\right)^2 + \frac{2}{k_i}(1 - \cos\phi_i)}, \tag{3.3}$$

where $i \in \{1, \ldots, n\}$. The work in [10, 11] shows how values for $\phi_i$ can be plotted as a function of the gain, $k_n$. Figure 3.2a shows representative minimum singular values of the return difference matrix. The universal gain margin / phase margin diagram, shown in Fig. 3.2b, can be used to determine the gain margins, phase margin, and margins for simultaneous combinations of gain and phase.

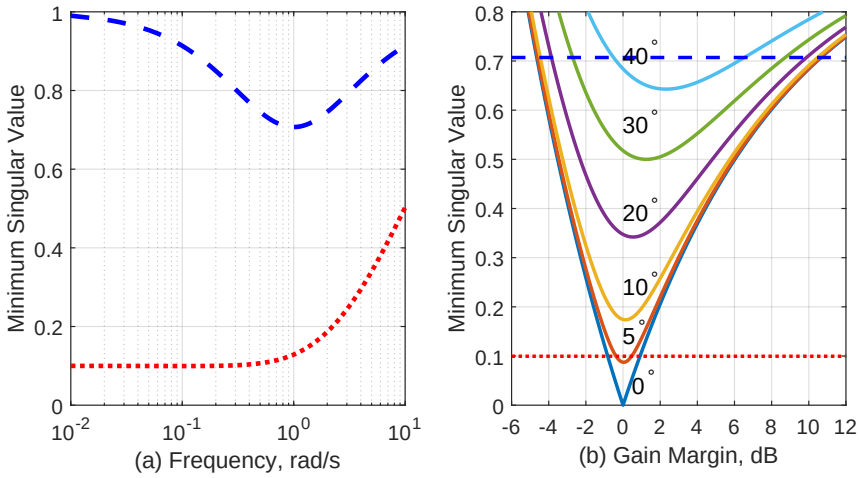


Figure 3.2: (a) Minimum singular values for two separate example problems. (b) The diagram used for universal gain margin and phase margin determination.

Figure 3.2b shows that the singular value corresponding to the blue dashed line has a lower gain margin of approximately $-4.5$ dB, an upper gain margin of $10.5$ db, and a phase margin of approximately $42°$. Similarly, the singular value corresponding to the red dotted line has a gain margin of approximately $\pm 1$ db and a phase margin of approximately $5°$. Combinations of phase and gain can be analyzed, using Fig. 3.2b, by selecting first a phase and then finding the corresponding gain margin or vice versa. Exact values for gain margins, phase margins, and combinations of gain and phase can be found by solving Eq. (3.3) directly. Note that although each of these two methods could be applied on a SISO system, the analyses in this paper are for MIMO systems. That is, the stability analyses, both the DM and the UGM, are performed to find the stability margins with respect to simultaneous perturbations in each loop for the inputs and the outputs of the plants, separately.

# Chapter 4

# CONTROL DESIGN

By now, after more than fifty years of development, it would be reasonable to assume that practically every major control law synthesis method and approach has been used in the study of active flutter suppression (AFS) [1]. Out of the many approaches possible, three were selected for study in the work here. First is one of the first engineering insight methods to be proposed - the ILAF approach [14–17]. The Static Output Feedback (SOF) approach [18–20] is a MIMO control law design method, known for years, in which state estimation is not necessary. The Polytechnic of Milan team has made the synthesis of SOF control laws more efficient and has significant experience with such laws. Finally, the LQR/LQG method was used because of its central role in modern control. The goals of the work here did not include finding the best control law synthesis method and comparing the control laws used for efficiency and performance. Rather, the focus was on following the process of synthesizing control laws from the early stage in the airplane design process where math models are still not optimized, the robustness measures evaluated with those control laws based on the early math models used, and then the study of those control laws' performance and robustness by experiments with hardware of the complexity and realism that would represent real aircraft development.

The ILAF approach is a classical control approach from the very early days of active control development for flexible flight vehicles. It is based on the insight that if velocity measurements can be linked to forces at the locations of those velocity measurements and in the opposite direction, a mechanism for adding damping to the structure by active control can be materialized that will be independent of the mode shapes of the configurations to be stabilized.

For optimizing SOF control laws, mathematical programming capabilities were developed at POLIMI, working with a well-posed optimization problem to yield optimal displacement and/or

velocity and/or acceleration gain matrices that are simple to grasp intuitively. In both the ILAF case and the SOF case, the flow in the control system closed loops is easy to understand, making it possible for the engineer to deviate, based on test performance, from original laws and to modify them quickly by changes that would be equivalent to adding stiffness and damping actively.

The effectiveness of any LQG control law depends, as is well known, on the selection of weight matrices in its performance metric and associated Kalman Filter and the number, quality and placement of sensors that would impact how well the state estimation process works. A particular selection of the LQR/LQG weight matrices was used here. The goal, as stated above, was not to find the best control law but just a good enough working control law that would allow analysis/test correlations and robustness studies.

In the following chapters, each control law synthesis process, as used in this work, will be concisely described. The control laws, as presented below, were designed only with the nominal model with no correction factor, as mentioned in chapter 2, applied to account for the uncertainty in aileron effectiveness.

### *4.1 Control Design - The ILAF Approach*

The approach adopted here is similar to the approach pursued by the authors of [4], who, despite much progress in controls technology since the early days of AFS, rightly felt that a re-evaluation of the simple, intuitive, quite straightforward ILAF approach merited a fresh study. In the present work, it was not only how ILAF laws would perform, but, mainly, how they would perform in the face of uncertainty that guided the effort.

As stated above, the theoretical basis for ILAF is that adding a force at a particular point proportional to the velocity at that point would increase the damping of all structural modes. There are practical concerns with the implementation of ILAF for active flutter suppression. These have been discussed over the years in publications on the implementation of the method. The most pertinent of these issues are:

1. Depending on the mode shapes affected, some locations will be more effective at adding

damping than others.

2. Control surfaces create a distributed loading rather than a point force at a particular location, though sensor placement can ameliorate this issue by improving the localized force-velocity relation.

The considerations above make the actuator and sensor selection a critical part of any ILAF-based design. With the understanding that the first symmetric modes were responsible for flutter, the trailing edge accelerometers on both sides of the control surfaces were chosen for feedback. As shown in the block diagram of Fig. 4.1, the outputs of trailing edge accelerometers were combined and used as an input to SISO-based ILAF controllers - one per side of the wind tunnel model.

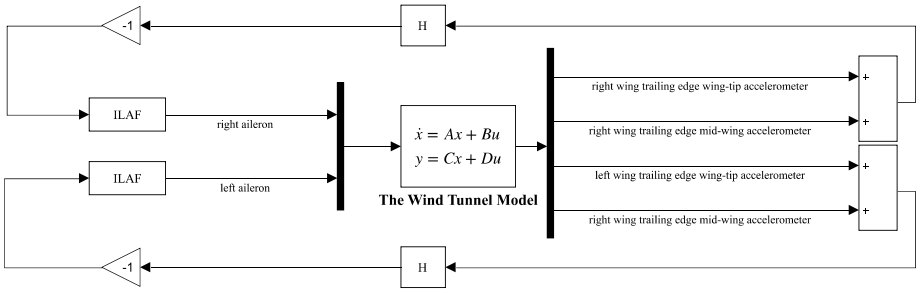


Figure 4.1: Control system block diagram for the active aeroelastic model under ILAF control.

In the diagram, the transfer function

$$H(s) = \frac{(2\pi \cdot 50)^2}{s^2 + 2(2\pi \cdot 50)s + (2\pi \cdot 50)^2} \tag{4.1}$$

is a second order low-pass filter with a 50 Hz cutoff frequency used to protect against high-frequency effects that the mathematical model does not capture well, as discussed in chapter 2. The low-pass filter was not used in the wind tunnel, as natural filtering of high-frequency effects is provided by the actual hardware.

In order to generate a force proportional to velocity, the accelerometer signals were integrated or, more specifically, approximately integrated [18–20]. The approximate integration, rather than the standard $\frac{1}{s}$ integration, is useful for removing low frequency sensor noise and any potential instabilities associated with the implementation of a pure integrator. Additionally, since each accelerometer measures a 1g offset due to gravity, a first order washout was added to remove this DC bias and any effect of gravity on the signals of the accelerometers in motions in which the accelerometers, due to the deformation of the model, tilt sideways from the vertical and read the resulting effects of gravitational acceleration.

The final form of the controller, before the selection of the gain, $K$, is shown in Eq. (4.2):

$$N(s) = \frac{s}{s+\pi} \cdot \frac{K \cdot s}{s^2 + 0.12s + 0.0036} \tag{4.2}$$

The parameters for the second order approximate integration were chosen according to [19]. Intuitively, these parameters are chosen such that the controller is rolling off as $\frac{1}{s}$ in the frequency range of interest. In this case, the frequency of interest, based on the mathematical model that was used for control law synthesis, is the flutter frequency at 40.8 rad/s.

The primary considerations in the selection of the gain, $K$, were to make the controller effective over a large range of speeds, lower and higher than the passive flutter speed. Standard root locus was used to find the gain, $K = 0.17$, that would lead to stable operation well below and above the open loop flutter speed. Fig. 4.2 shows the closed-loop root locus for vehicle speed from 15 m/s (green) to 60 m/s (red).

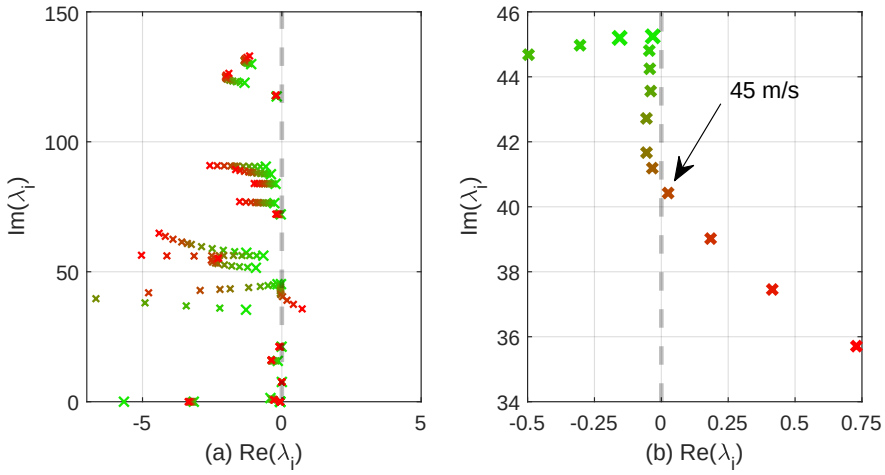


Figure 4.2: (a) ILAF controlled closed-loop root locus for air-speeds from 15 m/s (green) to 60 m/s (red). (b) Enlarged view showing the closed-loop flutter speed close to 45 m/s.

The ILAF controller was implemented in discrete-time using a Tustin transform from the continuous-time design. Since the sampling frequency used during testing was two orders of magnitude greater than the flutter frequency, continuous-time design methods, rather than discrete-time methods, are sufficiently accurate. The frequency response of the two-input loops and four-output loops, along with the loop-at-a-time margins, are presented in chapter 5.

## *4.2 Control Design - The Static Output Feedback Approach*

Static Output Feedback Control (SOF) [29] is a simple and effective approach to aeroservoelastic control law synthesis that has been studied and proven successful for active flutter suppression (AFS) and gust load alleviation (GLA) [18–20]. In the implementation of Static Output Feedback (SOF), the control input, $U(s)$, is obtained from measured responses, $Y(s)$, by means of a constant gain matrix, $G$, as $U(s) = GY(s)$. The behavior of the controller is then defined by the values of the elements of the gain matrix, which are computed by minimizing a weighted $H_2$ norm of the closed loop system.

In order to properly identify the closed loop transfer function whose norm is to be minimized, it

is necessary to select the performance output of interest, $z$, that is the set of system outputs whose responses need to be reduced. The performance output being distinct from the measurement output. For example, the performance output could be a particular modal velocity, or a particular combination of modal coordinates, or the internal loads in the structure in the case of a gust loads alleviation (GLA) controller. In order to obtain a well-posed optimization problem, it is also necessary to include the controller input, $u$, in the list of outputs taken into account in the norm of the closed loop system. The closed loop system input corresponds to disturbances that are expected to act upon the system. The minimization of the closed loop $H_2$ norm is equivalent to the minimization of a quadratic cost function associated with the norm of the control input and performance output [29, 30]:

$$J = \int_0^\infty \left[ z^T W_{zz} z + u^T W_{uu} u \right] dt, \tag{4.3}$$

where $W_{zz}$ and $W_{uu}$ are weight matrices defining the relative importance of input and output components. The computation of the gain matrix, $G$, that minimizes the cost function cannot be determined analytically; a numerical computation is required. Several algorithms have been proposed for that purpose [31, 32]. The one described in [20] is employed here. For the solution of the gain-finding optimization problem, a second-order Hessian-based algorithm is employed, for which the unknowns are just the elements of the gain matrix. Though not used in the present work that focuses on control gains, the vector of optimization unknowns can be extended to include any system parameter available for optimization.

The great simplicity of SOF controllers makes them attractive in many applications where simple control laws are desired. For example, they are particularly well suited for distributed systems, where actuator clusters are commanded only through feedback from a co-located set of sensors, i.e., only by groups of sensors located in the neighborhood of each actuator. To increase its overall performance, it would be easy to complement a SOF with a low-order dynamic regulator, designing the coupled static-dynamic controller through the same tools used for a purely static counterpart [33].

Owing to their simplicity, SOF regulators can also be used as backups, activated after a failure of a master system [34]. Another case in which SOF design techniques can be used is when some

parameters of an existing controller must be re-tuned while preserving its structure [35]. Finally, it is far simpler to schedule and interpolate the elements of a SOF gain matrix than the parameters of a dynamic controller, making it suitable, by gain scheduling, for varying operating conditions.

An example of an aeronautical application of SOF controllers is provided by the work of [36], where a SOF controller was used for the flutter suppression and gust alleviation of a HALE aircraft. The work also showed that a proper choice of the sensor locations provided results similar to those achievable by the use of an ideal full-state linear quadratic regulator. In the work described in [37], SOF flutter suppression was used based on a multi-model approach, i.e., weighting several different models within a single quadratic cost function, thus leading to a controller insensitive to the uncertainties structured within the accounted models. Another SOF active flutter suppression controller, using a direct digital design and including a size-constrained dynamic compensator, can be found in [33].

A common optimization approach in SOF is based on the solution of Lyapunov equations, having the closed-loop state matrix as coefficients. Within such a framework, many existing algorithms support a first-order gradient-based optimization, such as the legacy Levine–Athans algorithm [31], often revised as in [38], whereas a different approach can be found in work by Anderson and Moore [32].

Second-order optimization algorithms have also been proposed in [39–41], where the optimization is carried out on a state variance matrix instead of on a gain matrix, with the results being computationally very expensive when dealing with relatively large problems. The Anderson–Moore method [32] was modified to achieve superlinear convergence in [42] by introducing an approximation of the gain Hessian matrix. In [43] it was further enhanced with the computation of exact second derivatives of the cost function with respect to the gain matrix. Actually, its implementation was based on the iterative solution of a system of three coupled matrix equations, without any actual explicit calculation of the gain Hessian matrix. Another often-used solution method is the adoption of general-purpose state-of-the-art optimization functions, either unconstrained or constrained, for which the user has to provide the support to compute its own objective, gradient, and (possibly) Hessian

In this work, the POLIMI Lyapunov-based method was used [20], providing a simple and direct second-order approximation of the objective function by effectively calculating its true gain Hessian matrix, so that the optimization could be carried out as an iterative solution of the stationary condition through a simple Levenberg–Marquardt modified Newton–Raphson iteration. The algorithm is described in [20].

For the SOF control law synthesis of the wind tunnel aeroelastic model used here a control scheme based on eight outputs was used, i.e., the LE and TE tip and mid-wing accelerations. These accelerations were then individually run through a washout filter followed by an approximate integration.

The main challenge in the design of a flutter suppression controller using a SOF controller is that the gain design algorithm needs to be initialized with a stable system, for which the cost function is well adapted. This requires either starting with a stable system or already having a stabilizing controller to initialize the algorithm with. The system for which a flutter suppression controller is required is clearly not stable, and therefore it is not always easy to have a first-guess stabilizing controller.

In the present application an envelope expansion approach was used: The controller was first designed at a speed lower than the flutter speed. Then the flight speed was increased slightly, and the optimization was performed again using the controller obtained at the previous step as the starting point. The procedure was then repeated until the full speed range was covered, then obtaining a controller able to stabilize the system beyond the flutter speed.

No gain scheduling was implemented. The general Simulink scheme of the wind tunnel model implementation of the SOF controller is shown in Fig. 4.3. The controller was digitally implemented with a system working frequency equal to 1 kHz. Two control commands (outputs of the SOF control law) were used: the left and right ailerons. They were considered to be independent control surfaces. The control law was developed without taking advantage of the supposed symmetry of the model to address uncertainties in the construction of the model that prevented it from being perfectly symmetric. In Fig. 4.3, the gain matrix, $K$, is

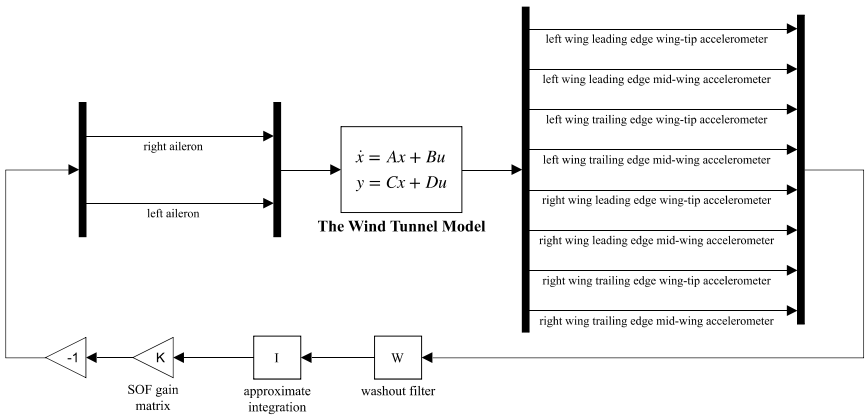


Figure 4.3: Static output feedback control structure.

$$K = \begin{bmatrix} 0.0242 & 0.0242 & 0.0211 & 0.0211 & 0.0614 & 0.0614 & 0.0569 & 0.0569 \\ 0.0242 & 0.0242 & 0.0211 & 0.0211 & 0.0614 & 0.0614 & 0.0569 & 0.0569 \end{bmatrix}, \tag{4.4}$$

which is the solution of the SOF optimization problem shown in Eq. (4.3). The approximate integration takes the form

$$I(s) = \frac{s}{s^2 + 1.257s + 0.3948}, \tag{4.5}$$

which is a simple high pass filter combined with a second-order system that attenuates low-frequency signals while appearing as a $\frac{1}{s}$ integrator at the 40.8 rad/s flutter frequency. The washout filter

$$W(s) = \frac{s}{s + 2\pi \cdot 3} \tag{4.6}$$

is a 3 Hz high-pass filter used to remove the 1g offset from gravity measured by the sensors. In addition, the high-pass filter is used to push the lightly damped 7.6 rad/s mode further into the left-half plane. As mentioned in chapter 2, the 7.6 rad/s mode does not appear in the physical hardware. Its presence in the mathematical model is due to inaccuracies in the math model at the very low frequency range as discussed above.

For wind-tunnel tests, the high-pass filter was lowered to 0.5 Hz. Though not shown in Fig. 4.3, the SOF controller used for analysis and simulation also contains a 50 Hz low-pass filter added

to attenuate the effects of high frequency effects in the math model where this model is inaccurate. The 50 Hz low-pass filter is only used for stability analyses and simulation and is not used during wind-tunnel tests.

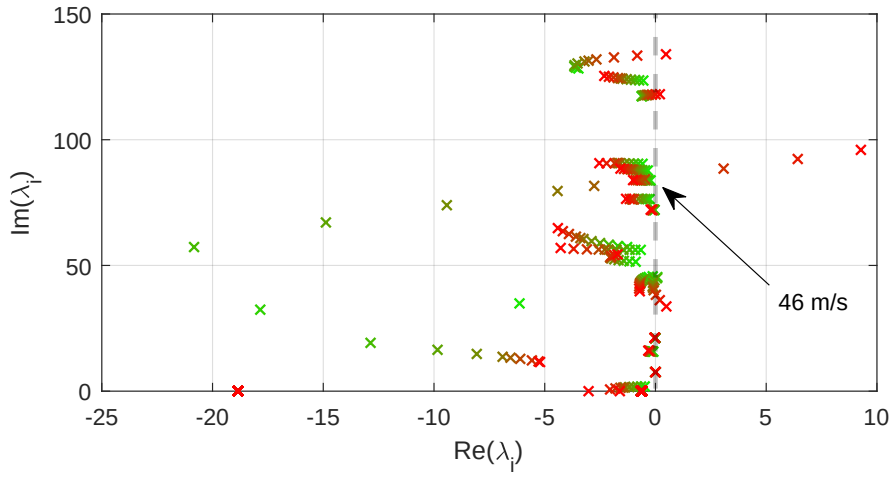


Figure 4.4: SOF controlled closed-loop root locus for air-speeds from 15 m/s (green) to 60 m/s (red).

Figure 4.4 shows the root locus with three branches crossing into the right-half plane (RHP) for the closed-loop SOF case. The first crossing occurs at a speed of approximately 46 m/s at a frequency of 80 rad/s, the second crossing occurs at a speed of 49 m/s at a frequency of 40 rad/s, and the third crossing occurs at a speed of 57 m/s at a frequency of 130 rad/s. The simulated flutter branch for the SOF-controlled system is the middle branch shown in Fig. 4.4, that occurs at a speed of 46 m/s and a frequency of 80 rad/s. Note that the flutter frequency of 12.7 Hz (80 rad/s) is quite close to the actuator bandwidth of 15 Hz. Consequently, the SOF-controlled system is expected to have difficulty stabilizing past the open-loop flutter speed. Any inaccuracy in the math model of the actuators or the unsteady aerodynamics of the control surfaces would affect this predicted critical instability. The SOF controller was discretized at 1000 Hz with a Tustin transform and implemented as a digital controller for the wind-tunnel tests. As will be shown later, this was, indeed, found by testing to be the case. Stability analyses for the SOF-controlled system

will follow in chapter 5.

### *4.3 Control Design - The LQG Approach*

The linear quadratic Gaussian (LQG) is a combination of a full-state linear quadratic regulator (LQR) for feedback regulation and a Kalman filter for state estimation. The separation principle allows the control and estimation portions to be designed separately, easing the burden on the engineer. The LQR problem is to find a control, $u$, that minimizes the quadratic cost function

$$J = \int_0^\infty (x^T Q x + u^T R u) dt, \tag{4.7}$$

where the vector of states is $x$ (in a standard state-space math model), and the matrices $Q$, and $R$ penalize the states and inputs, respectively. The effectiveness of LQR control laws depends on the weighting matrices, $Q$ and $R$, used for achieving the desired level of performance. The resulting optimal control law, $u^*$, is

$$u^* = -K\hat{x} = -R^{-1}B^T P\hat{x}, \tag{4.8}$$

where $P$ is the steady-state solution to an algebraic matrix Riccati equation, and $\hat{x}$ is the estimated state vector. The Kalman filter is the estimation dual of the LQR problem, as described in any textbook on modern control. Like the LQR problem, the effectiveness of Kalman filters depends on weighting matrices, $Q_E$ and $R_E$, used for tuning. In this case the matrices represent the process and measurement noise covariance matrices, respectively.

Among the first uses of LQG for active flutter suppression was Ref. [44], where the authors found the design procedure to be straightforward, but the controller order was considered high for digital implementation. Further research in [45] used model reduction to achieve lower order controllers and a modified design procedure [46] to recover the stability margins relative to full-state feedback.

The general control structure of the controllers developed in the work presented here can be seen in the block diagram shown in Fig. 4.5. The first LQR gain and Kalman filter were originally designed around a nominal plant created for the 42 m/s wind-tunnel speed. However, this set of

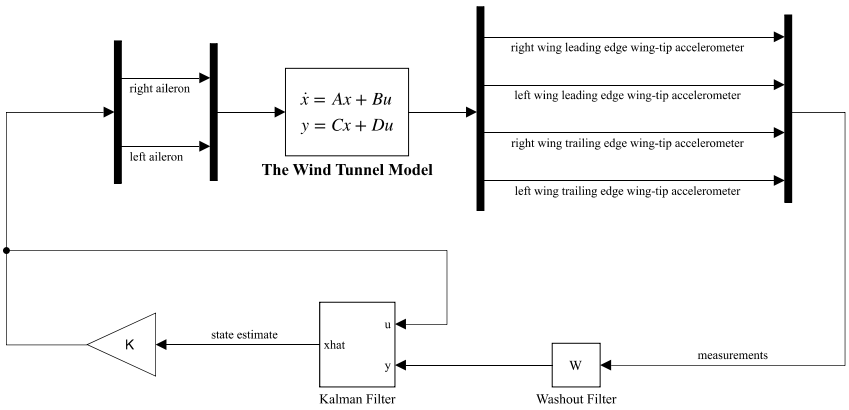


Figure 4.5: LQG control structure.

gains proved to be unstable in the wind tunnel. The LQR and Kalman filter were then redesigned using a nominal 45 m/s plant with the following design matrices

$$Q = (10^{-6})C^T C \tag{4.9}$$

$$R = 0.1I, \tag{4.10}$$

and

$$Q_E = I \tag{4.11}$$

$$R_E = 0.01I, \tag{4.12}$$

for the LQR and Kalman filter, respectively. The design matrices for the LQR were chosen to keep the wing-tip accelerations small, while using aileron deflections within the $\pm 20^\circ$ deflection limit. The Kalman filter design matrices, $Q_E$, and $R_E$, were chosen in an effort to minimize the difference between the theoretical and estimated Kalman filter performance verification metrics [47].

The measurements shown in Fig. 4.5 were chosen to be the four wing-tip accelerometers as they capture the desired features of the classical bending-torsional flutter mode exhibited by the wind tunnel model. The washout filter shown in Fig. 4.5 is the same as used by the ILAF controller. A closed loop root locus for air speeds from 15 m/s to 60 m/s can be seen in Fig. 4.6.

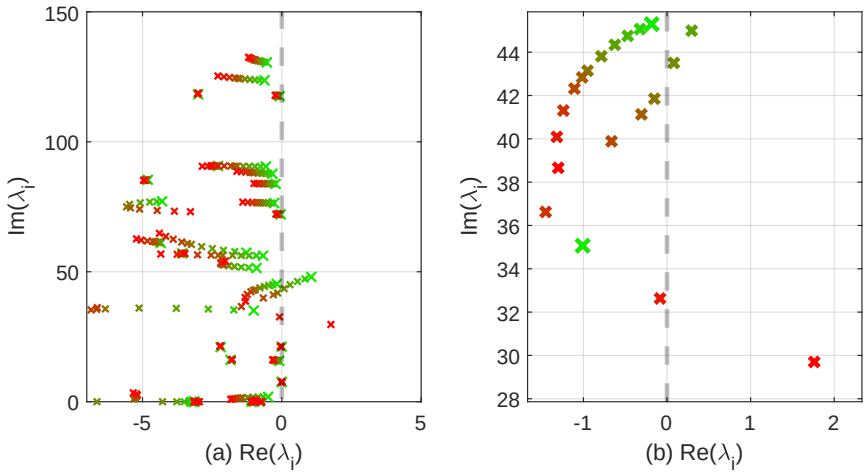


Figure 4.6: (a) LQG controlled closed-loop root locus for air-speeds from 15 m/s (green) to 60 m/s (red). (b) Enlarged view showing closed-loop stability between 36 m/s and 56 m/s.

Figure 4.6 shows the LQG controller developed for the tests to be stable from 35 m/s to approximately 55 m/s, far exceeding the open-loop flutter speed of 41.5 m/s. Unlike the ILAF and SOF-controlled systems, the LQG law here was not sensitive to inaccuracies in the math model of the system that led to the lightly damped modes at 1.2 Hz (7.6 rad/s) and 61 Hz (388 rad/s). As a consequence, analyses on the LQG cases proceed without the low-pass filter seen on the ILAF and SOF designs. The LQG controller was discretized at 1000 Hz with a Tustin transform and implemented as a digital controller for the wind-tunnel tests. Stability analyses for the LQG-controlled system will follow in chapter 5.

# Chapter 5

# ROBUSTNESS RESULTS

In the following chapter, the loop-at-a-time margins, the disk margin method, and the universal gain and phase margin methods were applied to the closed-loop wind tunnel model at both the inputs and outputs to the plant. The intent is to give a thorough picture of the stability margin properties of each controller that will be useful when studying correlations with experimental results. As the intent with the control design and wind tunnel tests is to show stability over a range of speeds, the DM method and UGM methods were applied across a range of speeds. These results show, qualitatively, how the multivariable gain and phase margins varied across speeds. Comparisons made across the three methods in the particular case of the flexible aeroelastic model project work described here add insights regarding stability margins for multi-loop systems in general. The reader will see in the following studies the sensitivities mentioned in chapter 2 for frequencies around 7.6 rad/s and 390 rad/s. Attempts were made in chapter 4 to filter these frequencies on the SOF and ILAF controllers, however, the following robustness analyses are sensitive to these frequencies. The sensitivity of the various methods to the model inaccuracy at the frequencies of 7.6 rad/s and 390 rad/s occurs with no greater magnitude than the dominant flutter mode. As a consequence, the stability analyses are not unduly affected. An important point to make is that, although disk margins and universal gain margins can be applied to single loops, the stability analyses carried out here were reserved entirely for multi-loop analyses.

## *5.1 Robustness Results - The ILAF Approach*

A robustness evaluation of the ILAF control law is presented in this chapter. The loop-at-a-time method and two multivariable stability margin methods are considered and compared.

### *5.1.1 Loop-at-a-time Margins*

Figure 5.1, below, shows the loop transfer functions calculated at the input and output of the aeroelastic plant at a wind tunnel speed of 42 m/s. These loops were calculated by closing all loops and then systematically opening one loop at a time and calculating the input/output response [21].

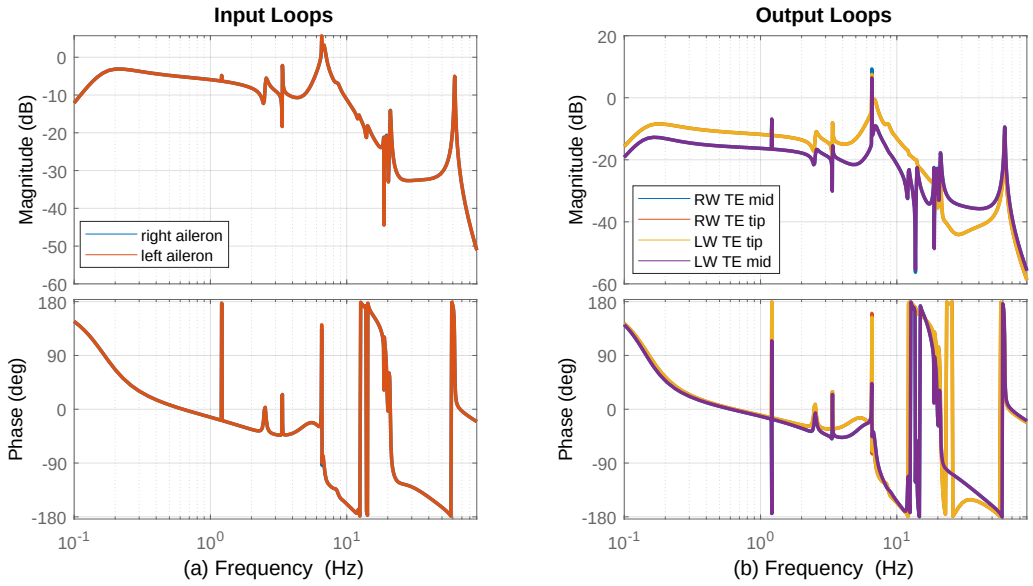


Figure 5.1: (a) Frequency response of the two-input loops at a wind-tunnel speed of 42 m/s. (b) Frequency response of the four-output loops at a wind-tunnel speed of 42 m/s.

The input loops shown in Fig. 5.1 can be seen to be nearly identical. Additionally, each input loop crosses the 0 dB line only near the flutter frequency. The high frequency mode seen at 60 Hz, as discussed in chapter 4.1, does not pose a stability risk as this mode does not manifest itself in the physical hardware, and the math model does not suitably capture behavior at this frequency range. Although Fig. 5.1b appears to show only two responses, all four responses are plotted. The two mid and two wing tip acceleration measurements, one on each side, have nearly identical responses. The gain difference seen in Fig. 5.1b is between the mid and tip accelerometers. The loop-at-a-time margins, calculated using the responses in Fig. 5.1 are shown in Table 5.1, below,

| | | Gain Margin [dB] | Phase Margin [°] |
|---|---|---|---|
| Output | $y_1$ | 7.11 | 112.0 |
| | $y_2$ | -6.19 | 92.7 |
| | $y_3$ | -7.2 | 88.0 |
| | $y_4$ | 7.1 | 115.0 |
| Input | $u_1$ | -4.01 | 61.7 |
| | $u_2$ | 4.29 | 61.8 |

Table 5.1: Minimum loop-at-a-time margins for the ILAF controlled system at a wind-tunnel speed of 42 m/s.

and are the minimum margins for each loop.

It is important to note that, although many of the margins in Table 5.1 are negative, this is not necessarily an indication of a problem. Rather it is an indication that some amount of control is required for stability. Negative gain margins, in particular, should be expected.

### *5.1.2 Disk Margin Method*

For the following results, MATLAB's Robust Control Toolbox was used to perform the disk margin analysis. The following figures show disk margins for the simulated system at the open loop flutter speed. Note that even though the flutter mechanism is symmetric, control is applied independently in closed-loop to the right and left wings.

Figure 5.2a shows a drastic decrease in the disk-based stability margins at frequencies of 7.6 rad/s, 40.8 rad/s, and 400 rad/s. These frequencies correspond to the low-frequency mode (see Fig. 5.1a), the flutter mode, and the previously discussed high-frequency characteristics, respectively. Figure 5.2a also shows the disk-based stability margins to be nearly identical when calculated at the inputs and outputs. The worst-case disk margins, for three different eccentricities, are shown

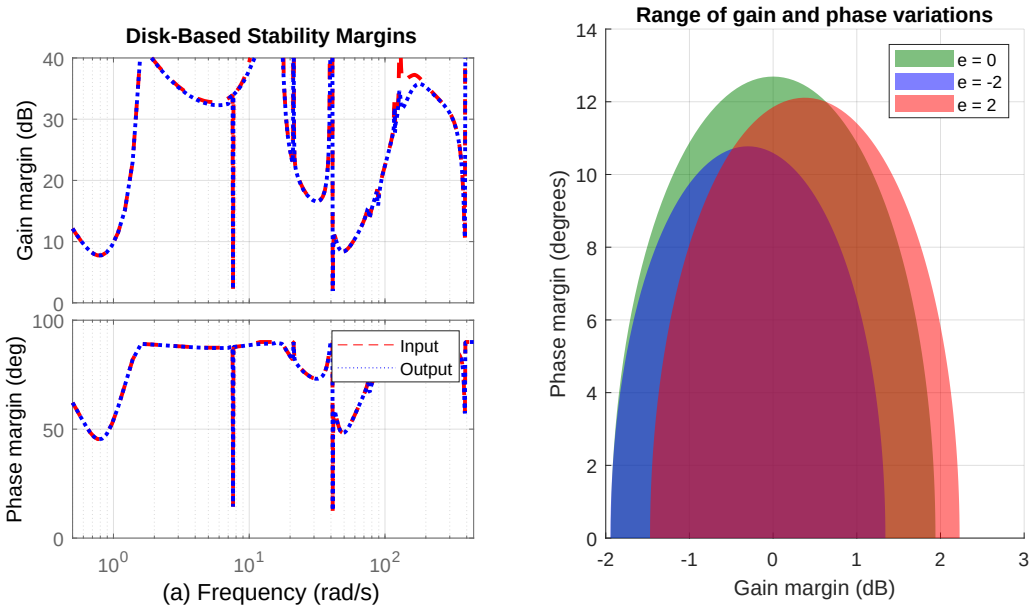


Figure 5.2: (a) Disk-based stability margins as a function of frequency. (b) Allowable gain and phase variations at the inputs and outputs for three different eccentricities.

in Fig. 5.2b for both the inputs and outputs.

For clarity, the worst-case disk margin can be understood as the smallest complex disk across all frequencies. Figure 5.2b shows that as the eccentricity, $e$, is increased, there is an increase in the allowable change in positive gain. However, when the eccentricity is decreased, there is no corresponding decrease in the amount of allowable gain. The interpretation of these results is that the closed-loop system is more robust to positive changes in gain than negative changes in gain.

The balanced disk margin results for the ILAF-controlled wind tunnel model are given below:

$$\begin{aligned} GM_{i,o} &= [-1.94, 1.94]\text{dB} \\ PM_{i,o} &= \pm 12.69^{\circ}, \end{aligned} \tag{5.1}$$

where the subscripts $i, o$ denote the inputs and outputs, respectively.

### *5.1.3 Universal Gain and Phase Margin Method*

Figure 5.3 shows the minimum singular values of the return difference matrix at the input and output of the closed-loop ILAF control wind tunnel model system calculated at a wind-tunnel speed of 42 m/s. The universal gain margin / phase margin diagram were developed for stability robustness assessment.

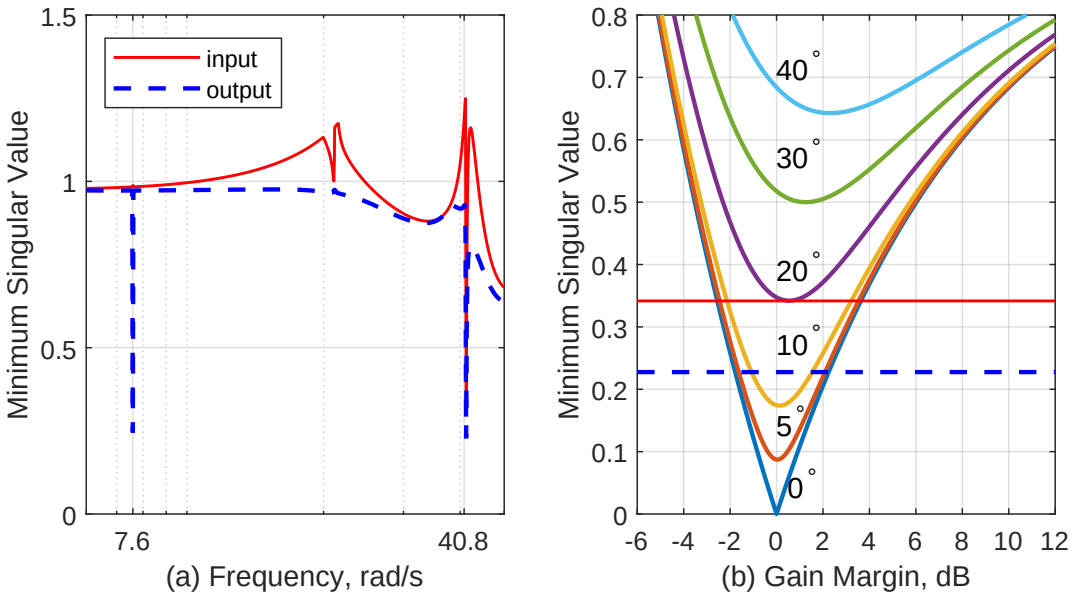


Figure 5.3: The ILAF controlled system at 42 m/s: (a) minimum singular values for the input and output return difference matrices; (b) the diagram used for universal gain margin and phase margin determination.

From Fig. 5.3, it can be seen that the phase margin is approximately $20^\circ$ at the inputs and approximately $13^\circ$ at the outputs, and the gain margin is approximately $\pm 3$ dB and $\pm 2$ dB, at the inputs and outputs respectively. Although the graphical approach represents a quick method of evaluating stability robustness in addition to giving a qualitative "feel" for the desirable and undesirable values for the minimum singular value, exact calculations for stability margins can also be carried out. In that case, Eq. (3.3) can be solved exactly for the gain margin, phase margin,

or simultaneous gain and phase margins. The exact stability values, calculated using Eq. (3.3), for the ILAF-controlled wind tunnel model are given below

$$\begin{aligned} GM_i &= [-2.55, 3.63]\text{dB} \\ PM_i &= 19.67^\circ \\ GM_o &= [-1.78, 2.24]\text{dB} \\ PM_o &= 13.06^\circ, \end{aligned} \tag{5.2}$$

where the subscripts $i$ and $o$ denote the stability margins calculated at the input and output, respectively.

Note that the authors of [10, 11] and the developer of the universal gain and phase margins had also developed expressions for the sensitivities of those margins to system and design variables and integrated those sensitivities into an optimization-based tool for the synthesis of control laws that would meet preset universal gain margin and phase margin constraints.

### *5.1.4 Summary of Stability Robustness Results at the Open-Loop Flutter Speed - The ILAF Approach*

The stability margin results are summarized in Table 5.2, below. Note that the loop-at-a-time margins are included in the summary only for the purposes of comparing the optimism, or conservativism, of the various methods. The loop-at-a-time margins are not a replacement for, nor should they be compared to, the multivariable methods. Additionally, the loop-at-a-time margins shown in Table 5.2 were the minimum values at the inputs and outputs shown in Table 5.1.

| | | DM | UGM | Loop-at-a-time |
|---|---|---|---|---|
| Input | Gain Margin, dB | $[-1.94, 1.94]$ | $[-2.55, 3.63]$ | -4.01 |
| | Phase Margin, ° | 12.69 | 19.67 | 61.7 |
| Output | Gain Margin, dB | $[-1.94, 1.94]$ | $[-1.78, 2.24]$ | -6.19 |
| | Phase Margin, ° | 12.69 | 13.06 | 88.0 |

Table 5.2: Stability margin summary for the ILAF controller.

### *5.1.5 Multivariable Stability Margins at Different Speeds - The ILAF Approach*

Figures 5.4 and 5.5, below, show how the multivariable stability margins vary with speed. Evident

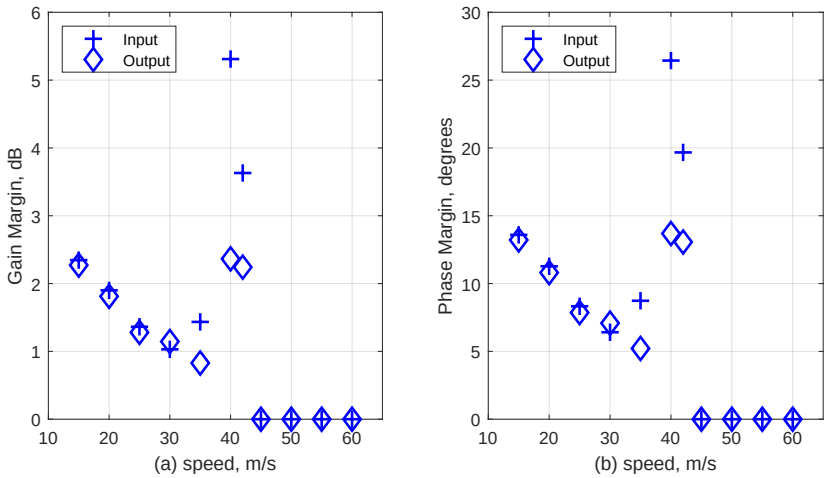


Figure 5.4: Universal Gain and Phase Margins for speeds from 15 m/s to 60 m/s: (a) Gain Margin, (b) Phase Margin.

in Fig. 5.5 is that the input and output disk margins are the same at each speed. The UGM method, Fig. 5.4, has very similar gain margins and phase margins when compared to the DM method.

However, it can be seen that the UGM has some differences between input and output phase and gain margins. These figures highlight how small the margins become below the open-loop flutter speed of 41.5 m/s and how the qualitative change of the stability margins across speed can be quite dramatic.

Note that in general an AFS control law designed to stabilize the system over a range of speeds may destabilize it below or above that range.

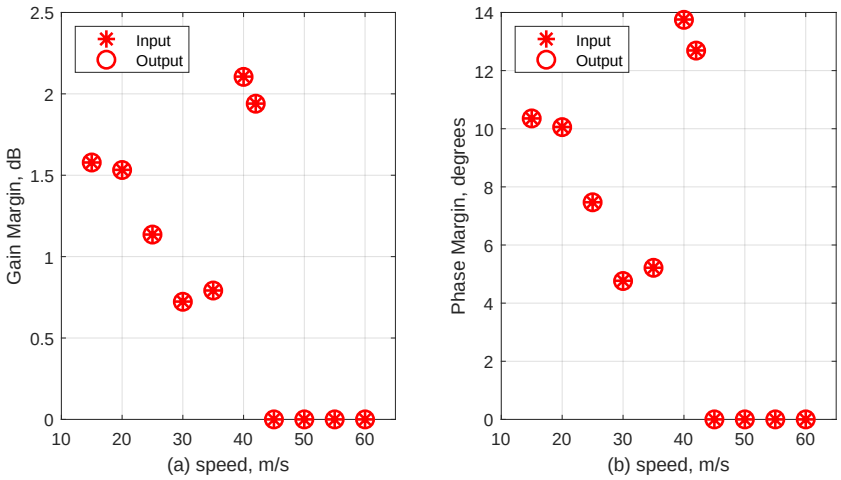


Figure 5.5: Balanced disk margins for speeds from 15 m/s to 60 m/s: (a) Gain Margin, (b) Phase Margin.

## *5.2 Robustness Results - The SOF Approach*

A robustness evaluation of the SOF control law is presented in this chapter. The loop-at-a-time method and two multivariable stability margin methods are considered and compared.

### *5.2.1 Loop-at-a-time Margins*

Figure 5.6, below, shows the loop transfer functions calculated at the input and output of the aeroelastic plant at a wind tunnel speed of 42 m/s. The responses were calculated with the relevant loop

open, while all other loops remained closed. Figure 5.6 shows the increased sensitivity at 1.2 Hz

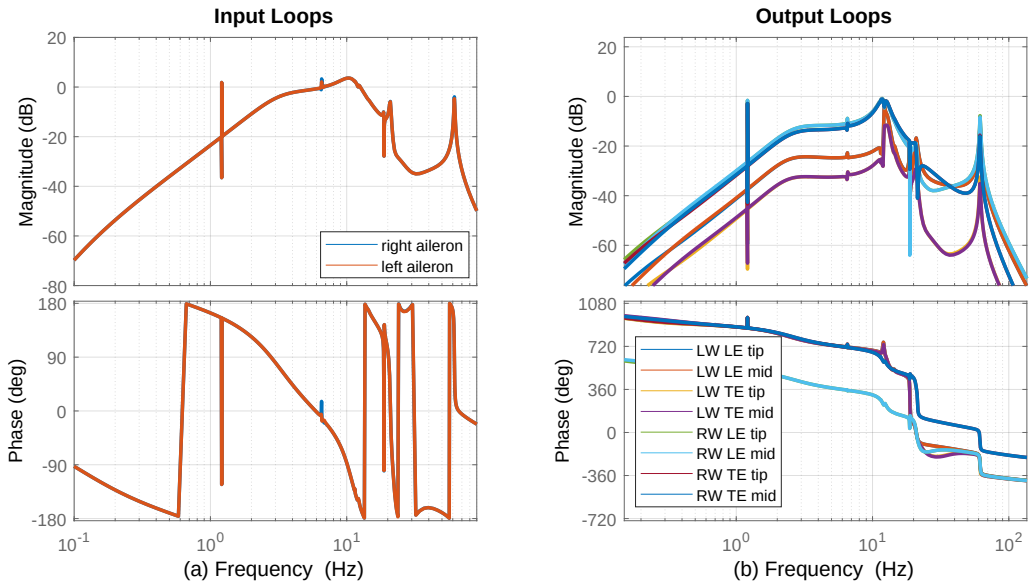


Figure 5.6: (a) Frequency response of the two-input loops at a wind-tunnel speed of 42 m/s. (b) Frequency response of the four-output loops at a wind-tunnel speed of 42 m/s.

and 61 Hz caused by the two structural modes mentioned in chapter 2. While Fig. 5.6a shows that the input loops are nearly identical, the output loops shown in Fig. 5.6b have a gain that varies over a range of approximately 20 dB. The variance in gain at the output is likely caused by the different sensor locations used for this control law, with similar sensors across the air-frame having similar gains. The loop-at-a-time margins, calculated using the responses in Fig. 5.6 are shown in Table 5.3, below.

| | | Gain Margin [dB] | Phase Margin [°] |
|---|---|---|---|
| Output | $y_1$ | 14.5 | $\infty$ |
| | $y_2$ | 14.8 | $\infty$ |
| | $y_3$ | 16.4 | $\infty$ |
| | $y_4$ | 16.5 | $\infty$ |
| | $y_5$ | 6.14 | $\infty$ |
| | $y_6$ | 6.14 | $\infty$ |
| | $y_7$ | 5.18 | $\infty$ |
| | $y_8$ | 5.18 | $\infty$ |
| Input | $u_1$ | 2.81 | 16.6 |
| | $u_2$ | 2.82 | 16.7 |

Table 5.3: Minimum loop-at-a-time margins for the SOF-controlled system at a wind-tunnel speed of 42 m/s.

The stability margins shown in Table 5.3 are the minimum margins for each loop. The similarity between stability margins shown in Table 5.3 can be understood when considering that the first four outputs, $y_1$ through $y_4$, are the mid-wing accelerometers located at the leading and trailing edge, while the last four outputs, $y_5$ through $y_8$, are the wip-tip accelerometers. The consistency among loop-at-a-time margins is due to the similarity in the physical location of the accelerometers.

### *5.2.2 Disk Margin Method*

Figure 5.7 shows the disk margin as a function of frequency and eccentricity for the SOF-controlled system. Note that by definition, the disk margin is defined with respect to the worst-case disk margin across all frequencies. Figure 5.7a shows that the worst-case disk margin likely occurs at either 7.6 rad/s or at 80 rad/s. Recall that the flutter frequency is predicted to be approximately 80

rad/s at a speed of 46 m/s from the middle branch on Fig. 4.4.

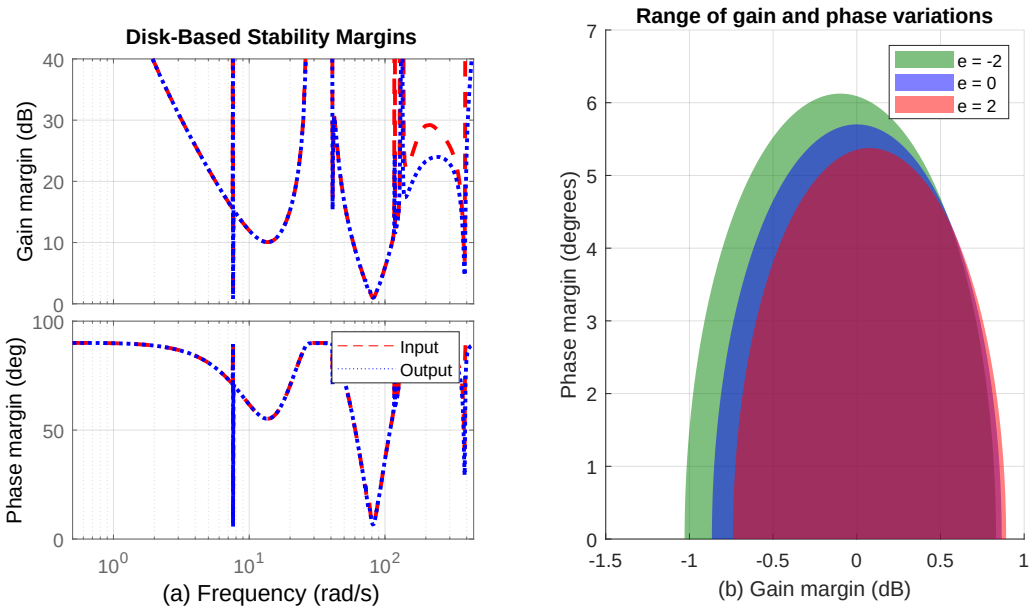


Figure 5.7: (a) Disk-based stability margins as a function of frequency. (b) Allowable gain and phase variations at the inputs and outputs for three different eccentricities.

Figure 5.7b shows the SOF-controlled system to be more resilient to negative than positive changes in gain. This conclusion is apparent as the decrease in eccentricity, shown in Fig. 5.7b, allows more perturbation in the negative direction than does a corresponding increase in eccentricity.

The balanced disk margin results for the SOF-controlled wind tunnel model are given below:

$$\begin{aligned} GM_{i,o} &= [-0.866, 0.866]\text{dB} \\ PM_{i,o} &= \pm 5.70^{\circ}, \end{aligned} \tag{5.3}$$

where the subscripts $i, o$ denote the inputs and outputs, respectively.

### *5.2.3 Universal Gain and Phase Margin Method*

Figure 5.8a shows the minimum singular values of the return difference matrix at the input and output of the SOF-controlled system calculated at a wind-tunnel speed of 42 m/s. The "universal diagram," Fig. 5.8, can be used to assess stability with respect to simultaneous perturbations in gain and phase and perturbations that exist only in gain or phase. From Fig. 5.8b, it can be seen

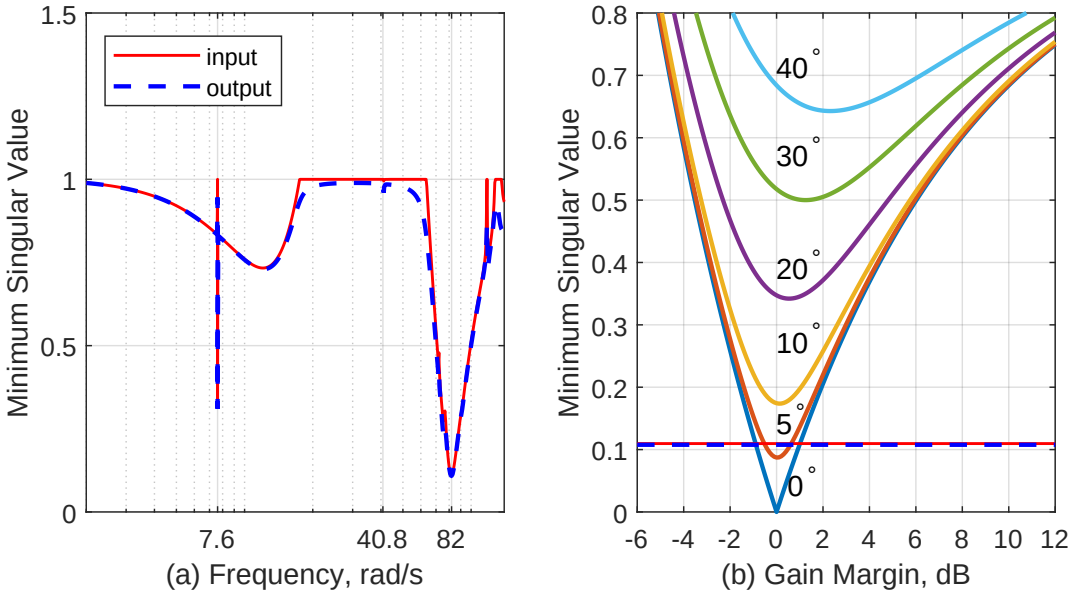


Figure 5.8: The SOF-controlled system at 42 m/s: (a) minimum singular values for the input and output return difference matrices; (b) the diagram used for universal gain margin and phase margin determination.

that the multi-loop stability margins at both the inputs and outputs are approximately $6^\circ$ and $\pm 1$ db.

Solving Eq. (3.3 directly) yields the results below:

$$\begin{aligned} GM_i &= [-0.90, 1.0]\text{dB} \\ PM_i &= 6.22^\circ \\ GM_o &= [-0.84, .93]\text{dB} \\ PM_o &= 5.83^\circ \end{aligned} \tag{5.4}$$

where the subscripts $i$ and $o$ denote the stability margins calculated at the input and output, respectively.

### *5.2.4 Summary of Stability Results at the Open-Loop Flutter Speed - The SOF Approach*

The stability margin results are summarized in Table 5.4, below. Similar to the analyses for the ILAF system, the minimum loop-at-a-time margins are included only to highlight the differences, qualitatively, between the loop-at-a-time margins and a multi-loop stability margin.

| | | DM | UGM | Loop-at-a-time |
|---|---|---|---|---|
| Input | Gain Margin, dB | $[-0.87, 0.87]$ | $[-0.90, 1.0]$ | 2.81 |
| | Phase Margin, $^\circ$ | 5.70 | 6.22 | 16.6 |
| Output | Gain Margin, dB | $[-0.87, 0.87]$ | $[-0.84, 0.93]$ | 5.18 |
| | Phase Margin, $^\circ$ | 5.70 | 5.83 | $\infty$ |

Table 5.4: Stability margin summary for the SOF controller.

### *5.2.5 Multivariable Stability Margins at Different Speeds - The SOF Approach*

Figures 5.9, and 5.10, below, show how the multivariable stability margins vary with speed. Note the reduction of robustness at speeds well below and above the range of speeds for which the SOF controller was designed.

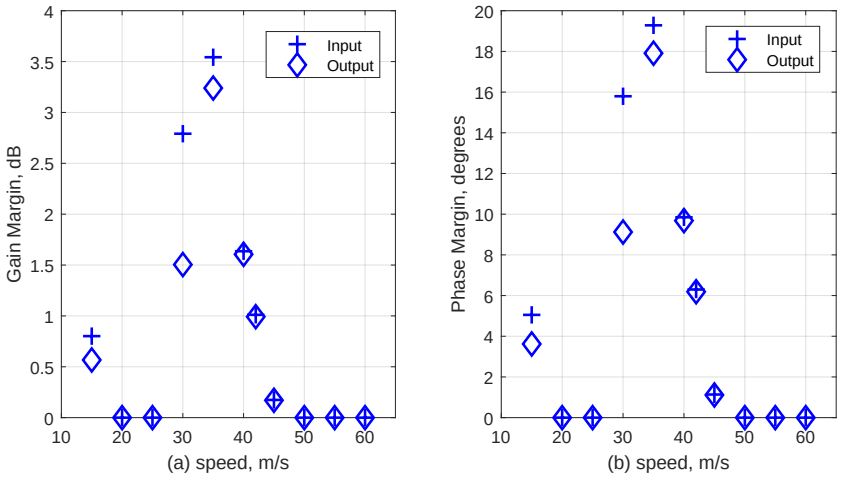


Figure 5.9: Universal Gain and Phase Margins for speeds from 15 m/s to 60 m/s: (a) Gain Margin, (b) Phase Margin.

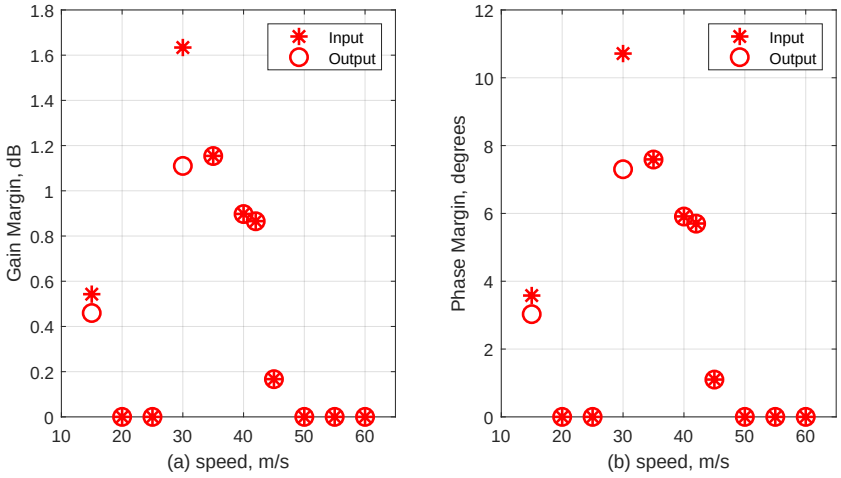


Figure 5.10: Balanced disk margins for speeds from 15 m/s to 60 m/s: (a) Gain Margin, (b) Phase Margin.

## *5.3 Robustness Results - The LQG Approach*

The stability results presented below, for the LQG-controlled system, follow those of the ILAF and SOF-controlled systems. Since introductions to the main themes have already been made, these results will be presented more concisely.

### *5.3.1 Loop-at-a-time Margins*

Figure 5.11 shows the loop response for the two-input loops and the four-output loops. Figure 5.11a

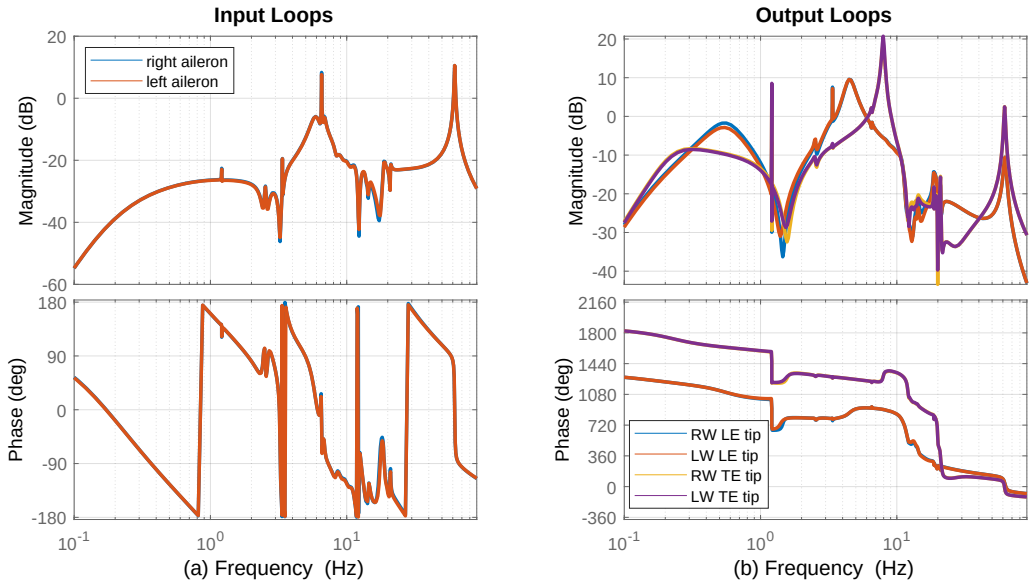


Figure 5.11: (a) Frequency response of the two-input loops at a wind-tunnel speed of 42 m/s. (b) Frequency response of the four-output loops at a wind-tunnel speed of 42 m/s.

shows the three common modes seen throughout these analyses; the 7.6 rad/s mode, the flutter mode at 40.8 rad/s, and the high-frequency mode at 390 rad/s. The responses shown in Fig. 5.11a are also nearly identical and have great attenuation above and below the flutter frequency. Figure 5.11b shows how similar outputs on opposite sides of the wind-tunnel model have nearly identical

responses. Further, the output-loop responses have much less attenuation across the frequency range of interest. The loop-at-a-time margins are shown below, in Table 5.5.

| | | Gain Margin [dB] | Phase Margin [°] |
|---|---|---|---|
| Output | $y_1$ | 5.7 | 21.6 |
| | $y_2$ | 5.8 | 21.6 |
| | $y_3$ | 4.4 | -22.6 |
| | $y_4$ | 4.4 | -22.7 |
| Input | $u_1$ | 22.8 | -104 |
| | $u_2$ | 22.8 | -104 |

Table 5.5: Minimum loop-at-a-time margins for the LQG-controlled system at a wind-tunnel speed of 42 m/s.

The multiple crossings of 0 dB, for gain, and $\pm 180$, for phase, shown in Fig. 5.11 indicate a few potential areas of instability, however, only the minimum margins were chosen for inclusion in Table 5.5.

### *5.3.2 Disk Margin Method*

Figure 5.12, below, shows the balanced disk margin as a function of frequency. As a reminder, the balanced disk margin has zero eccentricity and the allowable perturbations are centered around the nominal value of one, or 0 dB. Figure 5.12 shows the relative robustness of the input loops and the output loops across the frequency range of interest. Although the output loops have excellent margins for all frequencies, the input disk margins shown in Fig. 5.12 are low for frequencies from 1 rad/s to 100 rad/s.

Figure 5.13 shows the disk margins at the input and output for three eccentricities. Figure 5.13a shows the plant inputs to have very great robustness to perturbations in the positive direction, while

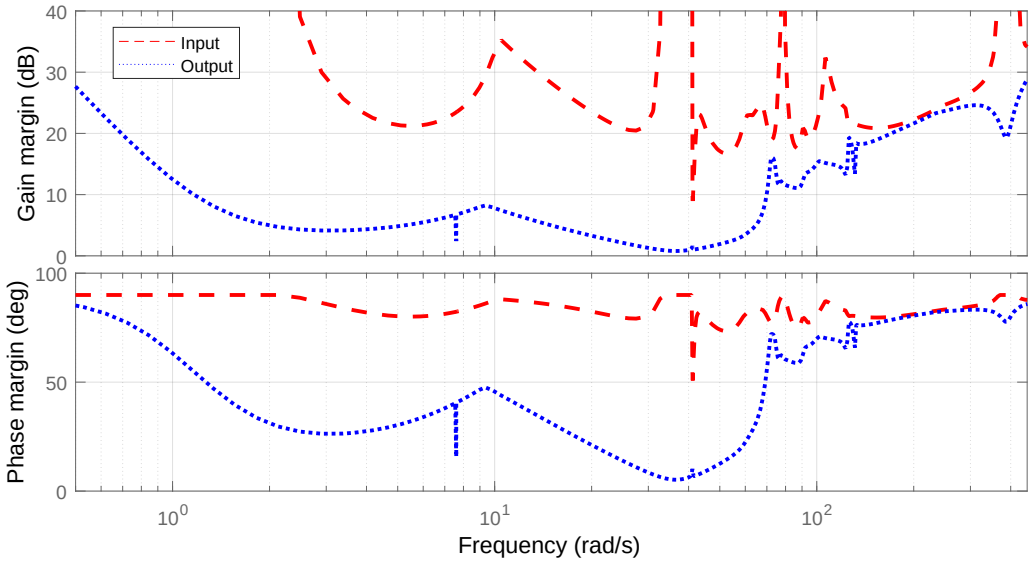


Figure 5.12: Input and output disk margins for the LQG-controlled system as a function of frequency.

still allowing perturbations in the negative direction, beyond the balanced case. Figure 5.13b shows the output disk margins to be quite small but also with little variance across eccentricities. The balanced disk margin results for the LQG-controlled wind tunnel model are:

$$\begin{aligned} GM_i &= [-8.96, 8.96]\text{dB} \\ PM_i &= \pm 50.78^\circ \\ GM_o &= [-0.7902, 0.7902]\text{dB} \\ PM_o &= \pm -5.20^\circ \end{aligned} \tag{5.5}$$

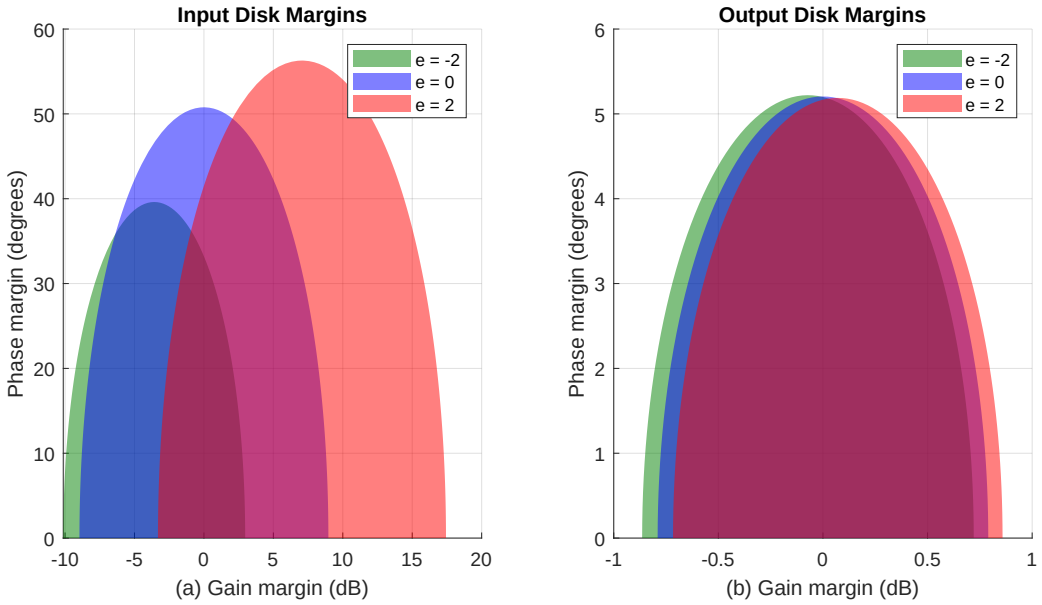


Figure 5.13: Disk margins for the LQG-controlled system for three different eccentricities at the (a) plant input, (b) plant output.

### *5.3.3 Universal Gain and Phase Margin Method*

Figure 5.14 shows the singular values of the return difference matrices and the corresponding "universal diagram" used for stability evaluations. Much like the disk margin analysis in Fig. 5.12, Fig. 5.14a shows the minimum singular value of the output return difference matrix to be small across a broad range, while the minimum singular value for the input return difference matrix is much higher. Figure 5.14b shows that the outputs have a multi-loop gain margin that is approximately 1 dB and a multi-loop phase margin of $5^\circ$, while the inputs have multi-loop margins of approximately -5 dB, 17 dB, and $50^\circ$ for the gain margin and phase margin, respectively. A summary of the universal gain and phase margins at the inputs and outputs is shown below:

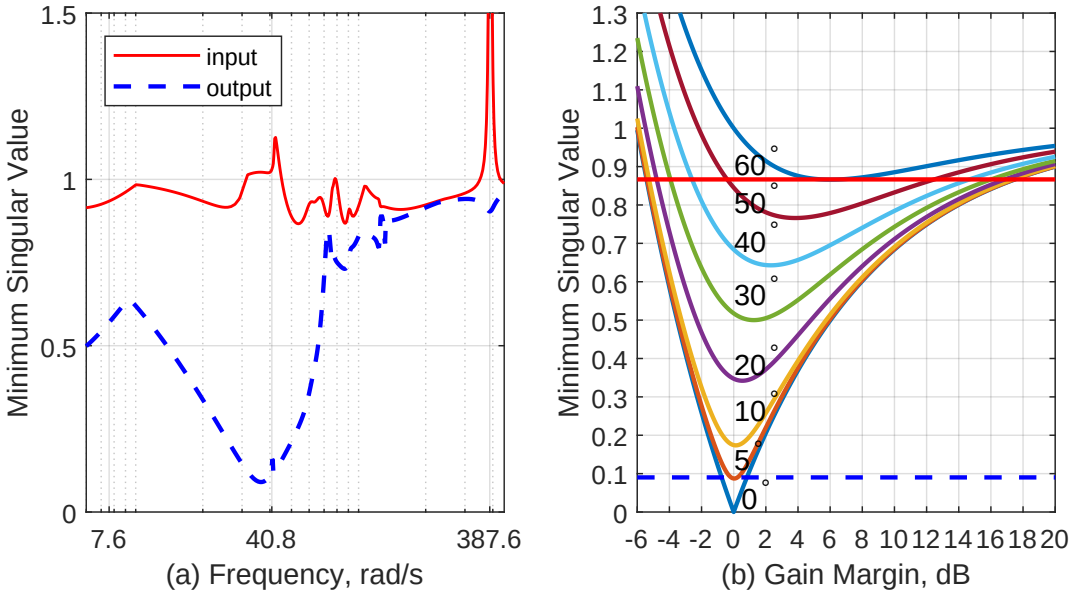


Figure 5.14: The LQG-controlled system at 42 m/s: (a): Minimum singular values for the input and output return difference matrices; (b): The diagram used for universal gain margin and phase margin determination.

$$
\begin{aligned}
GM_i &= [-5.42, 17.50]\text{dB} \\
PM_i &= 51.35^\circ \\
GM_o &= [-0.75, 0.82]\text{dB} \\
PM_o &= 5.17^\circ,
\end{aligned}
\tag{5.6}
$$

where the subscripts $i$ and $o$ denote the analyses at the inputs and outputs, respectively.

### *5.3.4 Summary of Stability Results at the Open-Loop Flutter Speed - The LQG Approach*

Table 5.6, below, shows the multi-loop margins, DM and UGM, alongside the minimum loop-at-a-time margin for the inputs and outputs. As shown in Table 5.6, the DM and UGM methods give similar results, particularly at the plant outputs. Worth noting is that, although the UGM method shows more robustness to positive changes in gain, the disk margin analysis shown in Fig. 5.13a

shows that, for increased eccentricity, the disk margin analysis can give similar results to those of the UGM method.

| | | DM | UGM | Loop-at-a-time |
|---|---|---|---|---|
| Input | Gain Margin, dB | $[-8.96, 8.96]$ | $[-5.42, 17.50]$ | 22.8 |
| | Phase Margin, $^\circ$ | 50.78 | 51.35 | -104 |
| Output | Gain Margin, dB | $[-0.7902, 0.7902]$ | $[-0.75, 0.82]$ | 4.4 |
| | Phase Margin, $^\circ$ | 5.20 | 5.17 | 21.6 |

Table 5.6: Stability margin summary at the open-loop flutter speed for the LQG-controlled system.

### *5.3.5 Multivariable Stability Margins at Different Speeds - The LQG Approach*

Figures 5.15, and 5.16 summarize the multi-loop stability results across a range of speeds. Also evident is the drastic change in stability for different speeds beyond the range of speeds at which the control law was designed, highlighting the need for some form of gain scheduling or a control synthesis method to account for the changing plant across the flight envelope of an airplane.

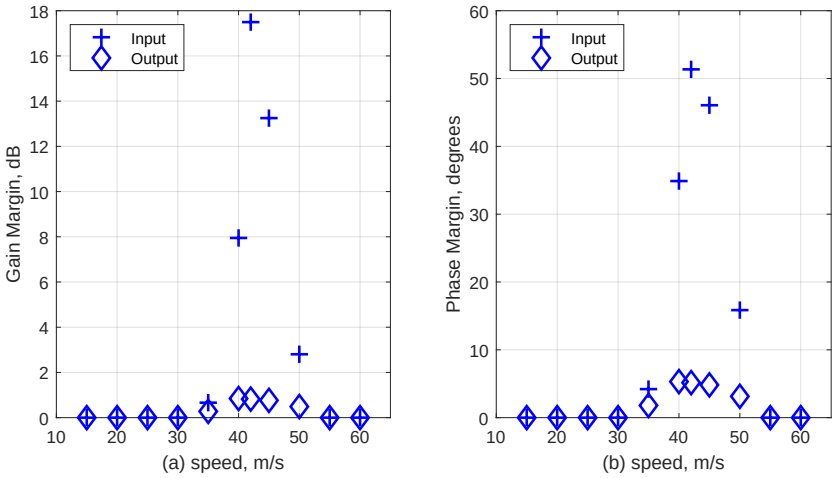


Figure 5.15: Universal Gain and Phase Margins for the LQG-controlled system for speeds from 15 m/s to 60 m/s: (a) Gain Margin, (b) Phase Margin.

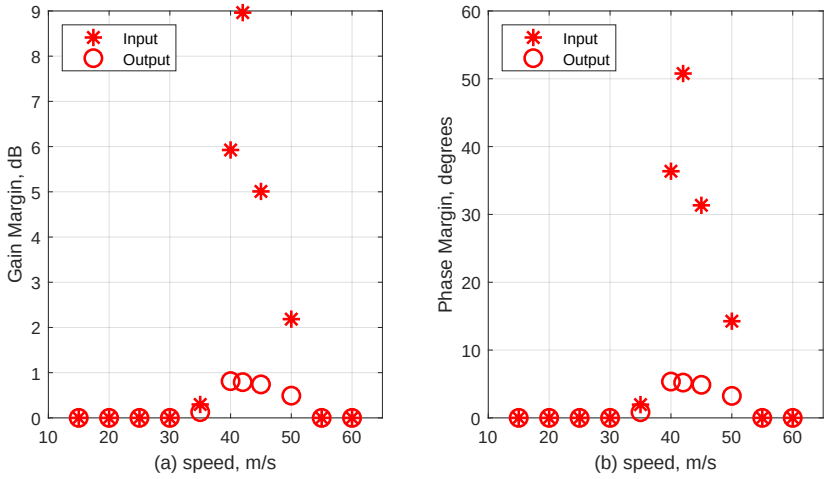


Figure 5.16: Balanced disk margins for the LQG-controlled system for speeds from 15 m/s to 60 m/s: (a) Gain Margin, (b) Phase Margin.

# Chapter 6

# EXPERIMENTAL RESULTS

Wind tunnel tests were conducted at the POLIMI large low-speed wind tunnel in Milan, Italy using the aeroservoelastic wind tunnel model described in chapter 2. The goals of the tests were to validate the mathematical models developed, to test the system over a range of speeds up to as much higher than the passive flutter speed as possible, and to evaluate the performance and robustness of the different control laws. Throughout the tests, band-limited white noise was added to the aileron commands to excite the model for system and flutter boundary identification. Each closed-loop system, the ILAF, the SOF, and the LQG, was evaluated for flutter envelope expansion and stability under gain and delay perturbations. The ILAF controller received an additional, more thorough, assessment of the stability properties by tests as a result of additional time that became available for wind tunnel tests. While an effort was made to be consistent across the control laws tested and the robustness tests each controller was subjected to were similar, they were not identical. The performance of each individual controller guided the direction of testing.

## *6.1 Experimental Results - The ILAF Approach*

Experiments were conducted on the ILAF-controlled system to establish the closed-loop flutter speed and to evaluate the system's stability to combinations of gains and delays at the inputs and outputs to the plant.

### *6.1.1 Closed-Loop Flutter Speed*

Figure 6.1, below, shows the time response of the ILAF-controlled closed loop system when active flutter suppression is cycled on and off while at the open-loop flutter speed of 41.5 m/s. As shown in Fig. 6.1, the ILAF-based active control worked very well to suppress flutter at the passive flutter

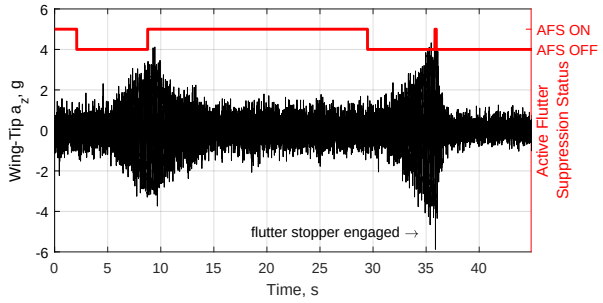


Figure 6.1: Time response of wing-tip accelerations with active flutter suppression cycled on and off.

speed. But if activated too late when the oscillations of the unstable system grew too large, the flutter stoppers engaged at their 4 g limit before the flutter suppression control could stabilize the system. The flutter stoppers proved crucial for safe exploration of the flutter boundary. Their high reliability made it possible to drive the system to the boundary of instability (open-loop and closed-loop) and deep into unstable regions again and again, which in a flight test without such safety mechanisms would be too dangerous to do.

The ILAF controller successfully stabilized the model at the open-loop flutter speed, as Fig. 6.1 shows. It was designed, however, to perform well over a range of speeds without gain scheduling: as low as 30 m/s and up to 43 m/s as shown in Fig. 6.2, below. Open and closed loop tests were

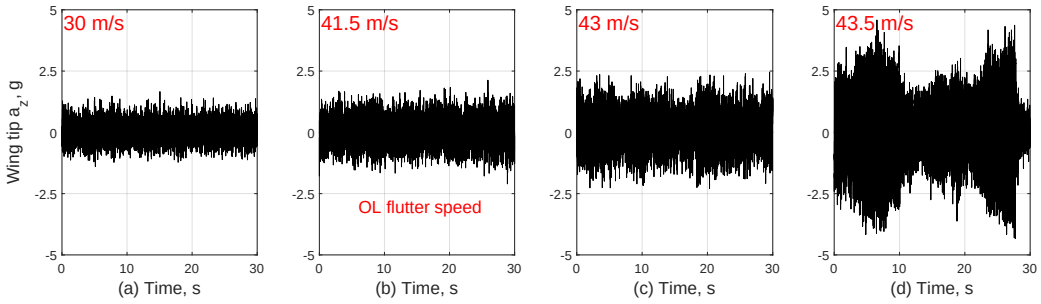


Figure 6.2: Time response of wing-tip accelerations for ILAF flutter suppression control operated from 30 m/s to 43.5 m/s.

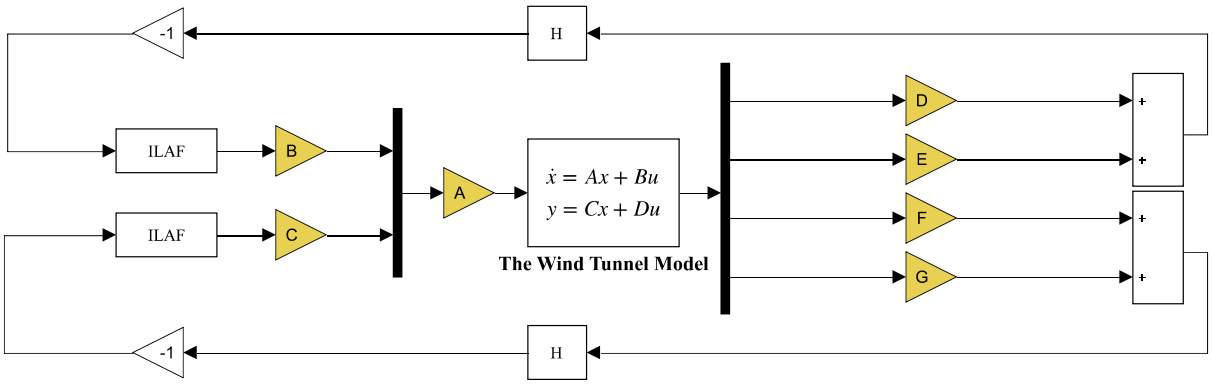


Figure 6.3: Test points for injecting gains and delays into the closed loop system.

performed at many intermediate speeds. The speeds shown in Fig. 6.2 were chosen to demonstrate the ILAF controller performance at the lowest speed for which it was designed, then at the open-loop flutter speed, and finally, very close to the closed-loop stability boundary and at the closed-loop stability boundary at 43.5 m/sec where the flutter stoppers had to automatically engage. These results compare favorably with those of Fig. 4.2, which showed closed-loop stability from 15 m/s to, approximately, 45 m/s.

Figure 6.2 also shows a dramatic increase in oscillation levels and a certain beating nature of the oscillation at 43.5 m/s. The test was constrained by the activation of the flutter stoppers, and so in-depth study of the closed-loop dynamics at and slightly beyond instability could not be pursued. The beating behavior seen in Fig. 6.2 is likely caused by several poles being close in frequency. Figure 4.2 shows several sets of poles with the potential to explain this behavior.

### *6.1.2 Stability Evaluation*

In order to evaluate robustness of the closed loop systems, gains and system delays were deliberately changed during the test. Figure 6.3 shows the points at which those gain and delay changes were made. For these studies, the model was operating at the open-loop flutter speed of 41.5 m/s. Test point A, in Fig. 6.3, was used to change gains, delays, and simultaneously change gains and

delays to both aileron inputs. Figure 6.4 shows the time response of a wing-tip accelerometer for gain changes at test point A. The gains were decreased in increments of 0.1 (relative to the nom-

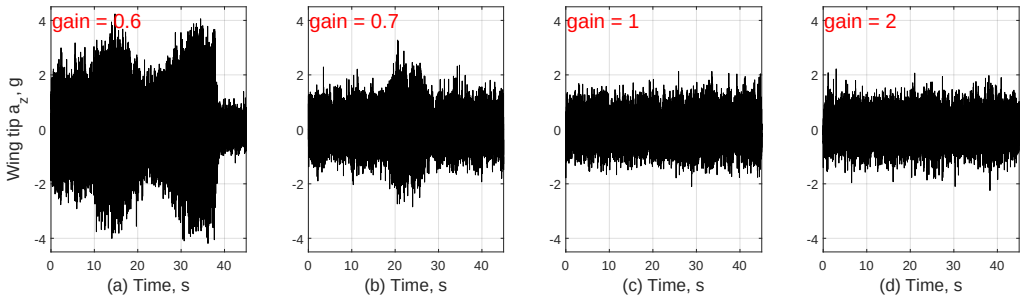


Figure 6.4: Time response of wing-tip accelerations to gain changes at both aileron inputs. Wind tunnel speed = 41.5 m/sec

inal values) at test-point A, shown in Fig. 6.3, until instability was reached, and then increased gradually. If instability was not reached up to a factor of two increase, no further gain increase was attempted.

Figure 6.4 shows a degradation in performance for a gain of 0.7 and instability for a gain of 0.6 applied to both aileron inputs. Qualitatively, Fig. 6.4 also shows there to be a slight general decrease of the acceleration's response to wind tunnel turbulence for the gain of 2.0 at both aileron inputs. The results shown in Fig. 6.4 compare well with both the disk margin analysis and universal gain margin analysis of chapter 5. As a reminder, chapter 5 showed the wind tunnel model to be stable under ILAF control for gains in the ranges of [-1.94,1.94] dB, and [-2.55,3.63] dB using the disk margin and universal gain margin analyses, respectively. Figure 6.5 shows the results of varying the delays applied to both aileron inputs.

The closed-loop system is shown in Fig. 6.5 to be stable (but with higher response to excitation by tunnel's turbulence) for a delay of 5 ms, and unstable for a delay of 10 ms applied to both aileron inputs. Using the flutter frequency of 40.8 m/s, delays of 5 ms and 10 ms correspond to phase changes of 11.7° and 23.4°, respectively. The multi-loop phase margins for the ILAF-controlled system were found to be $12.69°$ and $19.67°$ using the disk margin and universal gain

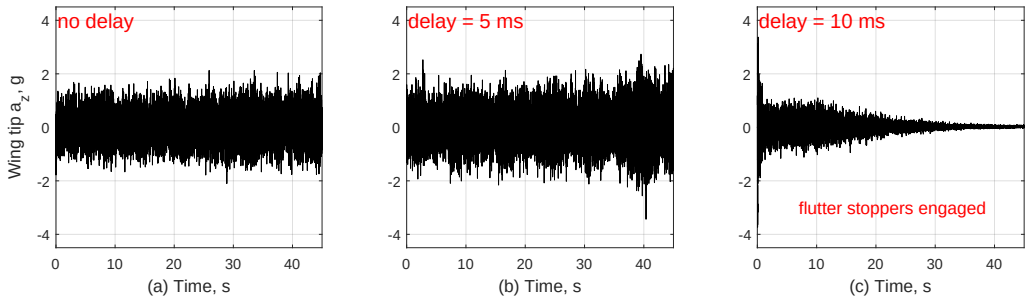


Figure 6.5: Time response of wing-tip accelerations for delays added to both aileron inputs. Wind tunnel speed = 41.5 m/sec.

margin method, respectively. The results shown here are not overly conservative as the destabilizing phase delay occurred only marginally outside the regions of guaranteed stability calculated using either method.

The last stability test performed at test point A was to change the gain while applying a constant 5 ms delay. The results can be seen in Fig. 6.6. Despite the 5 ms delay applied at test point A,

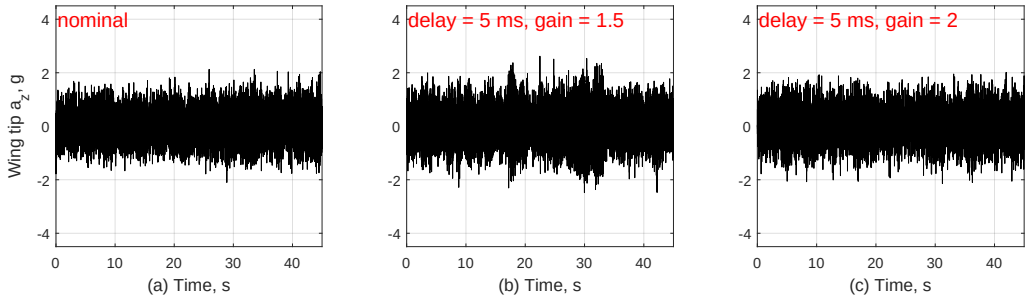


Figure 6.6: Time response of wing-tip accelerations for simultaneous gains and delays added to both aileron inputs. Speed = 41.5 m/sec.

the qualitative behavior shown in Fig. 6.6 indicates somewhat lower levels of accelerations due to tunnel turbulence for the gain increase factor of 2.0. This test shows stability to a simultaneous gain of 2.0 and phase change of 11.7° at both aileron inputs. A gain of 2.0 and a phase change

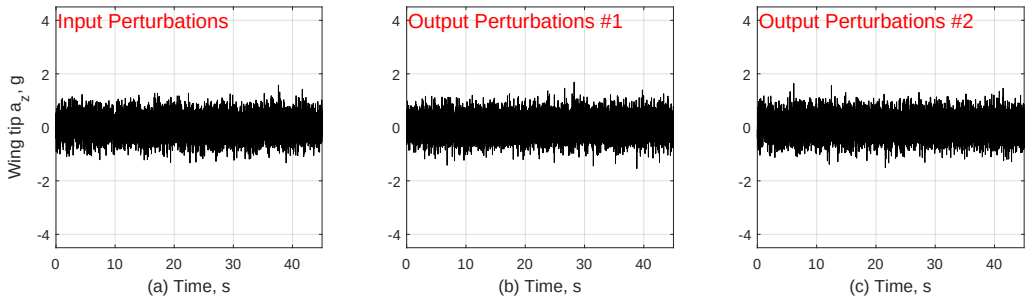


Figure 6.7: Figure (a): Gains and delays at test points B and C. Figures (b) and (c): Gains and delays at test points D through G. Wind-tunnel speed = 41.5 m/sec.

of 11.7° are outside the guaranteed stability region for simultaneous changes in gain and delay, see Table 5.2, however, this does not necessarily mean the methods are overly conservative. A perturbation may exist with a smaller phase change for a particular direction of gains. Whether or not the method is conservative depends on if the instabilities found using the various methods, DM or UGM, are physically possible or are of practical concern.

This last test shows a certain level of robustness to simultaneous delays and increased gains. However, lacking in these tests were independent perturbations at the inputs and outputs. The following tests will evaluate the robustness of the ILAF-controlled system to simultaneous changes in gain and delays at the inputs and outputs using the test points shown in Fig. 6.3.

### *6.1.3 Stability for Simultaneous Control Law Perturbations*

To evaluate robustness to independent control law perturbations at the inputs and outputs, tests were conducted at points B through G using independent gains and delays based on the stability analyses performed in chapter 5. Note that control law perturbations implemented during the tests are equivalent to changes in the dynamic system in closed loop, with the nominal control law being active.

Figure 6.7a shows the time response of a wing-tip accelerometer to a control law perturbation consisting of a 2 ms delay and gains of 0.9 and 1.122 at the left and right ailerons, respectively. Fig-

ure 6.7b shows the time response for a delay on all outputs of 2 ms combined with gain changes of 1.168, 0.86, 0.86 and 1.168 on the first through fourth outputs, respectively. Figure 6.7c shows the time response for the same changes in gain but for a larger 5 ms delay. The DM and UGM methods both show, see Fig. 5.2 and Fig. 5.3, that the closed-loop system should be stable for simultaneous perturbations of approximately 5° and $\pm 1$ dB on both aileron inputs or the measurement outputs. The stability results shown in Fig. 6.7 are in agreement with these analyses.

## *6.2 Experimental Results - The SOF Approach*

Tests were conducted in the wind tunnel to evaluate the closed-loop flutter speed of the SOF-controlled system and to evaluate the robustness to changes in delay and changes in gains. Correlations between these test results and equivalent tests performed on the numerical model will be presented in chapter 7.

### *6.2.1 Closed-Loop Flutter Speed*

Figure 6.8 shows that the closed loop flutter speed for the SOF-controlled system was 50 m/s. The predicted flutter speed, based on Fig. 4.4, was 46 m/s.

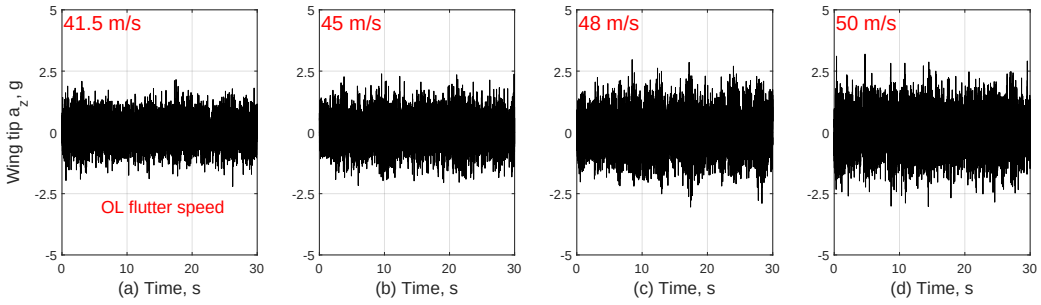


Figure 6.8: Time response of wing-tip accelerations for SOF flutter suppression control operated from 41.5 m/s to 50 m/s.

### *6.2.2 Stability Robustness Evaluation*

The stability robustness evaluations performed on the SOF-controlled system were more limited than on the ILAF-controlled system. Tests were conducted for changes in gains on the aileron inputs for wind-tunnel speeds of 41.5 m/s, 46 m/s, and 50 m/s. A delay test was also conducted on the aileron inputs at a wind-tunnel speed of 41.5 m/s.

Figure 6.9 shows the SOF-controlled system to be stable for changes in gain at the aileron inputs of 0.2, 0.4, and the nominal value of 1.0. The margins at the open loop flutter speed can be seen in Table 5.4. For completeness, the margins shown for the SOF-controlled system at the open-loop flutter speed are $[-0.87, 0.87]$, and $[-0.90, 1.0]$, using the DM and UGM methods, respectively. These margins correspond to gain decreases of 0.9 and gain increases of 1.1 at the aileron inputs. The results shown in Fig. 6.9 show the closed-loop system to be much more resilient to negative gain changes than predicted by the multi-loop margins.

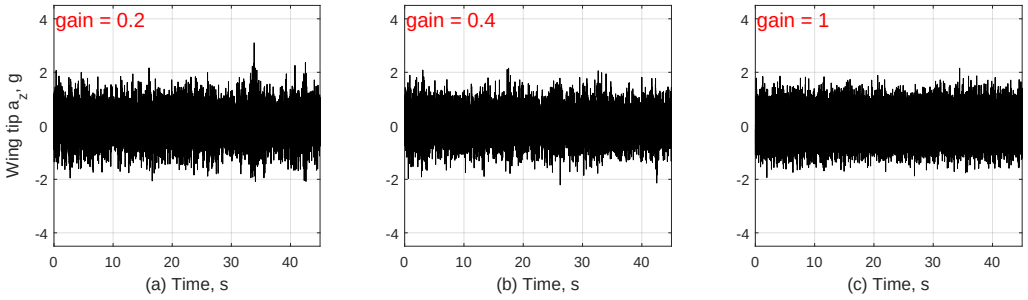


Figure 6.9: Time response of wing-tip accelerations to gain changes at both aileron inputs. Wind tunnel speed = 41.5 m/sec.

Figure 6.10 shows the results of gain changes applied to the aileron inputs at a wind-tunnel speed of 46 m/s. Stability is shown in Fig. 6.10 for decreases in gain of 0.4 and 0.6. The margins for a wind-tunnel speed of 46 m/s can be approximated by looking at Fig. 5.10a; these margins are $\approx \pm 0.2$ dB for both the DM and UGM methods. Considering that the physical model was stable at 50 m/s (Fig. 6.8) while the numerical/analytical model predicted a closed-loop flutter speed of 46 m/s, the discrepancies in these stability evaluations are likely caused by inaccuracies in modeling

rather than conservativeness of the methods. Highlighting the apparent model inaccuracy, the gain changes conducted at a wind-tunnel speed of 50 m/s (Fig. 6.11) cannot be correlated with the numerical model as the numerical model shows instability at this speed.

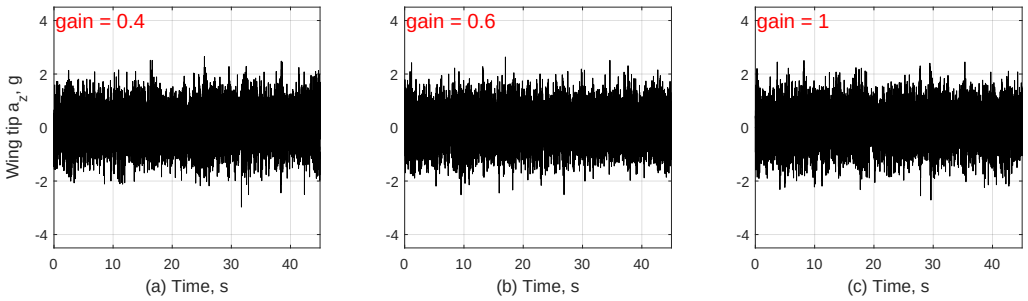


Figure 6.10: Time response of wing-tip accelerations to gain changes at both aileron inputs. Wind tunnel speed = 46 m/sec.

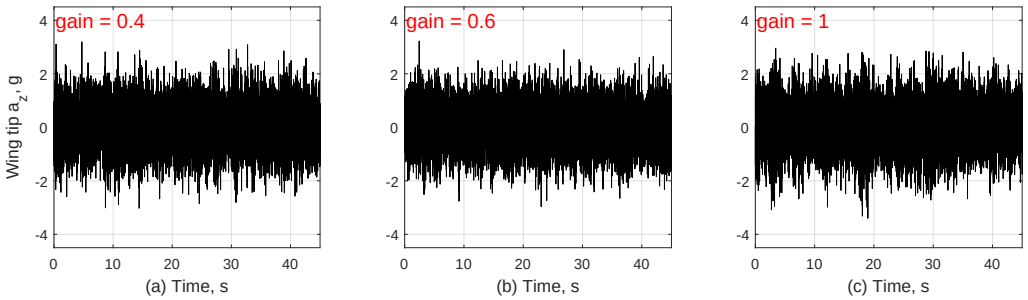


Figure 6.11: Time response of wing-tip accelerations to gain changes at both aileron inputs. Wind tunnel speed = 50 m/sec.

Figure 6.12 shows the SOF-controlled system to be stable for input delays of 3 ms and 5 ms added to the aileron inputs. With a flutter speed of 40.8 rad/s, 3 ms and 5 ms delay correspond to phase changes of 7 and 11.7 degrees, respectively. The stability margins for the SOF-controlled system at a wind-tunnel speed of 41.5 m/s, see Table 5.4, show multi-loop phase margins of 5.70 and 6.22 degrees for the DM and UGM methods, respectively. The amount of delay added to the

aileron inputs was outside the predicted multi-loop margins, resulting in good correlation between test and analysis.

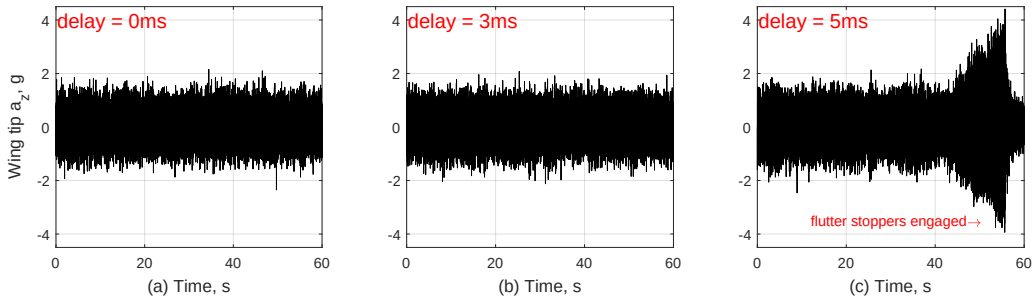


Figure 6.12: Time response of wing-tip accelerations to delays at both aileron inputs. Wind tunnel speed = 41.5 m/sec.

## *6.3 Experimental Results - The LQG Approach*

Wind-tunnel tests were conducted for the LQG-controlled system to evaluate the closed-loop flutter speed and the robustness properties of the closed-loop system. The robustness properties were evaluated through the application of gains and delays on the aileron inputs. Correlations between these test results and equivalent tests performed on the numerical model will be presented in chapter 7.

### *6.3.1 Closed-loop Flutter Speed*

The closed-loop flutter speed for the LQG-controlled system was found to be 46.5 m/s, based on the results presented in Fig. 6.13. These results are considerably different than the predicted closed-loop flutter speed, see Fig. 4.6, of 56 m/s. This discrepancy may be accounted for by considering the correction factor, mentioned in chapter 2, used to account for aileron effectiveness. The correction factor will be considered in chapter 7.

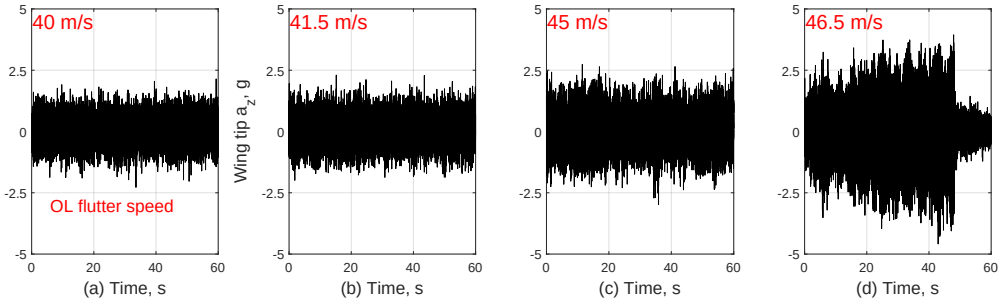


Figure 6.13: Time response of wing-tip accelerations for LQG flutter suppression control operated from 40 m/s to 46.5 m/s.

### *6.3.2 Stability Evaluation*

The stability tests on the LQG-controlled system consisted of gain and delay changes at the open-loop flutter speed, and a test of delays for various speeds. Figure 6.14 shows the LQG-controlled system to be stable for gain changes of 0.9 and 1.2. These gain changes are well within the margins shown for the LQG-controlled system in Table 5.6. Figure 6.15 shows stability for 5ms and 10ms delays added to the aileron inputs. For context, 5 ms and 10 ms delays correspond to phase changes at the flutter frequency of approximately 12 degrees and 24 degrees, respectively. The multi-loop phase margins for the LQG-controlled system, shown in Table 5.6, are $50.78^\circ$ and $51.38^\circ$ for the DM and UGM methods, respectively. The delays were clearly well within the predicted multi-loop margins.

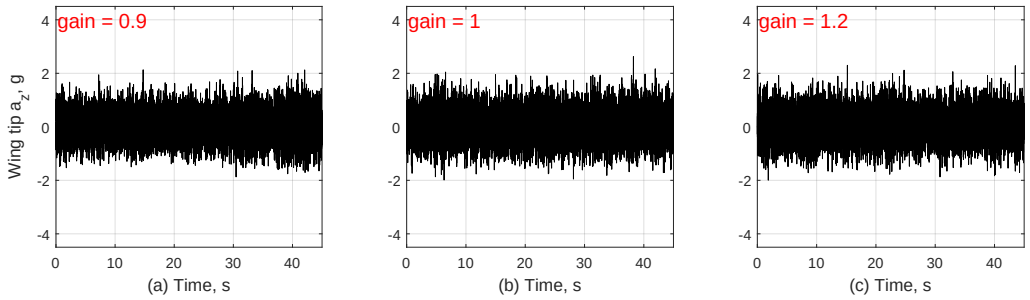


Figure 6.14: Gain changes at the inputs at the open-loop flutter speed of 41.5 m/s.

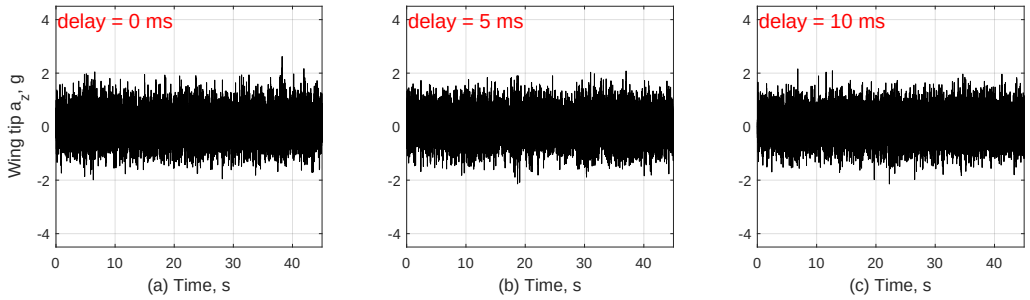


Figure 6.15: Delay changes at the inputs at the open-loop flutter speed of 41.5 m/s.

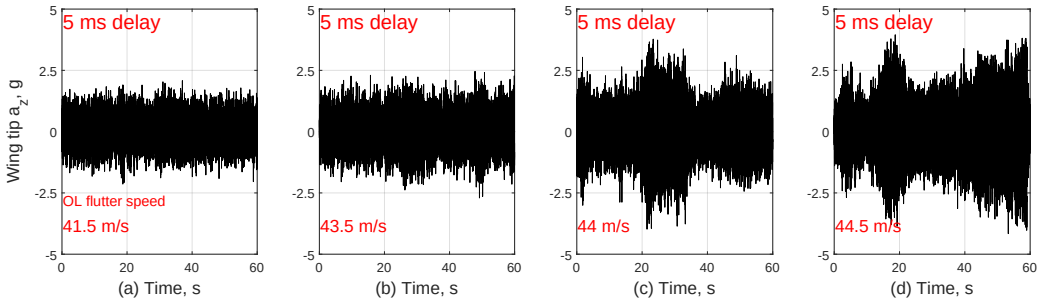


Figure 6.16: Delay of 5 ms to control inputs for speeds from 41.5 m/s to 44.5 m/s.

Figure 6.16 shows the effects of a 5 ms delay for the wind-tunnel speeds of 41.5 m/s, 43.5 m/s, 44 m/s, and 44.5 m/s. Qualitatively, the response seen in Fig. 6.16c seems to indicate that the stability margins have been severely degraded. A further increase in speed by 0.5 m/s, seen in Fig. 6.16d, bring about instability. As seen in Fig. 5.16 and 5.15, the multi-loop phase margins are never lower than $30^\circ$ across these speeds. The 5 ms delay added to the aileron inputs corresponds to an approximate phase margin, at the relevant modal frequency, of $12^\circ$. This represents a difference in multi-loop phase margin of at least 18 degrees. The conclusion is that there likely exists a significant mismatch between the model and the physical hardware at the wind-tunnel speeds beyond the OL flutter speed.

# Chapter 7
# ANALYSIS AND EXPERIMENT CORRELATION

Some discussion of the correlation between analysis and tests has already been presented. This chapter will further explore the correlation between the analyses performed using the analytical model from chapters 2 and 5 and the experimental results presented in chapter 6. The first comparison, and possibly the most straightforward, is to compare the predicted closed-loop flutter speed for each method to the closed-loop flutter speed observed in the wind-tunnel tests. This will be followed by correlations between the robustness tests performed in the wind tunnel and the multivariable stability margins and perturbed closed-loop root loci based on the analytical model. The perturbed closed-loop root loci, to be presented below, were created with gains variations and, when necessary, pade approximations for the delays.

## *7.1 Correlation in Closed-Loop Flutter Speed*

The table below summarizes the prediction results from chapter 4 and the measured results from chapter 6. Note that the experimentally-found closed-loop flutter speed for the LQG-controlled system had a gain of 1.2, rather than a gain of 1.0. This is because with the LQG controller on, no instability was reached within the range of wind tunnel speeds planned for the reported tests.

The predicted closed-loop flutter speed for the LQG-controlled system, shown in Table 7.1, has been updated to reflect a gain of 1.2 on both aileron inputs. The average of the percent differences seen in Table 7.1 is $9.8\%$. As mentioned in chapter 2, the original aeroelastic model that was used for synthesizing the control laws did not include aerodynamic corrections – in particular a correction factor to account for the aileron aerodynamic effectiveness. Short of carrying out dedicated tests in the wind tunnel or detailed CFD simulations for establishing aerodynamic correction factors, Ref. [48] was used. Results for plain flaps in that reference lead to a 0.8 correction factor for

| | Predicted (m/s) | Measured (m/s) | Percent Difference (%) |
|---|---|---|---|
| ILAF | 44 | 43.5 | 1.1 |
| SOF | 46 | 50 | 8.0 |
| LQG | 56 | 46.5 | 20.4 |

Table 7.1: Summary of predicted and measured closed-loop flutter speed for the ILAF, SOF, and LQG-controlled systems.

the effect of aileron motions on the generalized aerodynamic force changes. Adding a correction factor of 0.8 to the aileron inputs gives the results shown in Table 7.2, below.

| | Updated Prediction (m/s) | Measured (m/s) | Percent Difference (%) |
|---|---|---|---|
| ILAF | 42 | 43.5 | 3.4 |
| SOF | 48 | 50 | 4.0 |
| LQG | 54 | 46.5 | 9.7 |

Table 7.2: Summary of predicted and measured closed-loop flutter speed for the ILAF, SOF, and LQG-controlled systems using an aileron-effectiveness correction factor of 0.8.

The average of the percent differences seen in Table 7.2 is $7.8\%$. It is clear that the correction factor applied to the aileron inputs improved the accuracy of the predicted closed-loop flutter speeds. The development of "best" correction factors to be used requires more analysis and test efforts. However, in the context of the present work it is not that essential since this work studies how control laws with their robustness measures developed for aeroelastic systems that are known to have uncertainties in their mathematical models perform in reality.

This is not to say, of course, that the designers can be sloppy in developing the system math models that they will use for designing active controls for. What this means, in the context of

aeroservoelastic active control, is that the closed loop systems are to be designed anticipating uncertainties in particular areas such as aerodynamic forces, natural frequencies, mode shapes, actuator dynamics, etc. starting with reasonable mathematical models capable of capturing the essential physics involved. The uncertainties in the models should be addressed by making the control laws robust.

Note also that in the numerical studies and tests presented here, variation of wind tunnel speeds, plus variations of gains and delays in the closed loop system had the effect of capturing how a nominal control law, based on an imperfect math model, would perform in the face of speed, aerodynamic force, and structural dynamic / actuation variations.

### *7.2 Correlation Analysis - ILAF*

In this chapter, the individual wind-tunnel experiments performed on the ILAF-controlled system will be compared to similar tests on the analytical model and compared against the multivariable stability margins. In order to compare the effects of delays and gains on the closed loop system, closed-loop root loci have been constructed using third-order pade approximations for the time delays, and gains have been added, when appropriate, to the inputs and outputs of the plant. The intent with the closed-loop root loci is to capture the conditions that occurred during the wind-tunnel tests. The aileron aerodynamic correction factor added in the previous chapter has an obvious effect on the robustness tests previously conducted. These robustness results were recalculated using the updated model with the 0.8 correction factor on the aileron inputs. The robustness results are presented concisely below. Worthy of reiterating at this time is that the analytical model contains modes at approximately 7.6 rad/s and 390 rad/s that do not exist on the physical model (due to inaccuracies of the math model at those frequencies, as discussed above). Instabilities caused by these modes in the following perturbed root loci will receive little attention as the intent is to correlate the known, 40 rad/s, flutter mode with the experimental results. Updated closed-loop root locus, disk margin analysis, and universal gain margin analysis are presented below in Figs. 7.1, 7.2, and 7.3, respectively. The closed-loop flutter speed shown in Fig. 7.1 is approximately 42 m/s, which is less than the measured closed-loop flutter speed, see Fig. 6.2, of 43.5 m/s. The multivariable

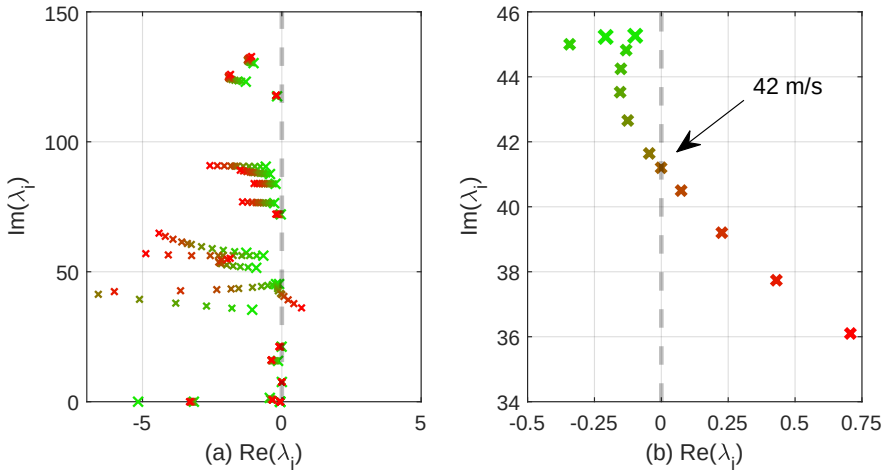


Figure 7.1: Figure (a): ILAF-controlled closed-loop root locus for the updated model with 0.8 correction factor for air-speeds from 15 m/s (green) to 60 m/s (red). Figure (b): Enlarged view showing the closed-loop flutter speed close to 42 m/s.

stability margins shown in Figs. 7.2, and 7.3 are considerably less than those determined in chapter 5. Exercising the power of the eccentricity parameter in the DM analysis, Fig. 7.2 shows that the closed-loop system is much more resilient to positive changes in gain than negative changes and, in fact, is robust to combinations of increases in both gain and phase. A summary of the stability properties for the nominal system with the 0.8 correction factor is shown below in Table 7.3. The margins shown in Fig. 7.2, and 7.3 reflect the proximity of the speed at which they were calculated to the speed at which instability is lost. Not surprisingly the system is very sensitive to parameter variations at these conditions.

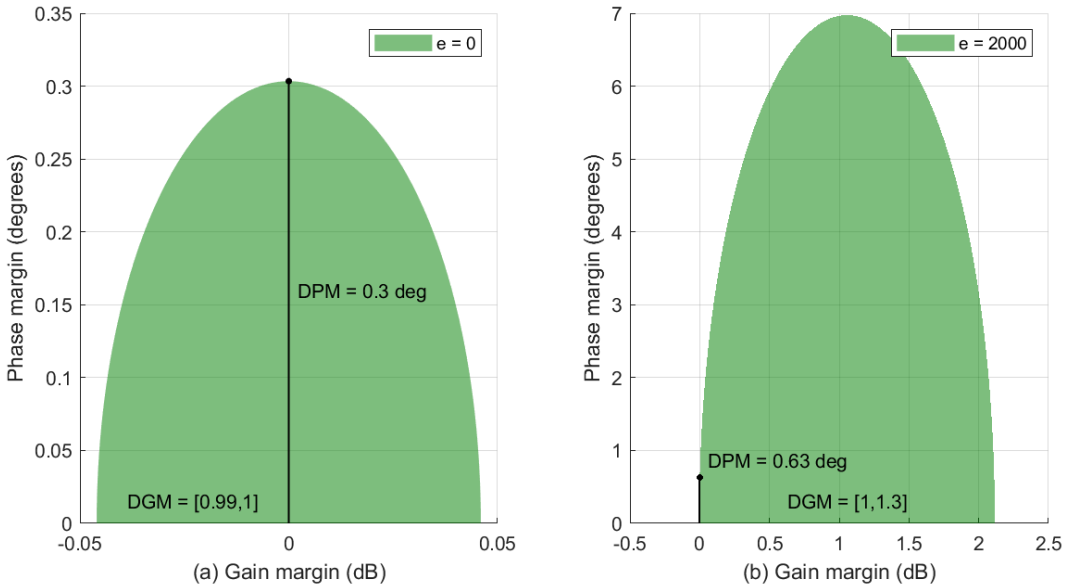


Figure 7.2: Input disk margins for the ILAF-controlled system with the 0.8 correction factor at a wind-tunnel speed of 42 m/s: (a) balanced disk margin, and (b) Disk margin heavily-skewed towards positive changes in gain.

| | | DM | UGM |
|---|---|---|---|
| Input | Gain Margin, dB | $[-0.0460, 0.0460]$ | $[-0.0460, 0.0463]$ |
| | Phase Margin, $^\circ$ | 0.30 | 0.30 |
| Output | Gain Margin, dB | $[-0.0460, 0.0460]$ | $[-0.0419, 0.0421]$ |
| | Phase Margin, $^\circ$ | 0.30 | 0.28 |

Table 7.3: Stability margin summary for the ILAF controller with the 0.8 correction factor added to the aileron inputs at a wind-tunnel speed of 42 m/s.

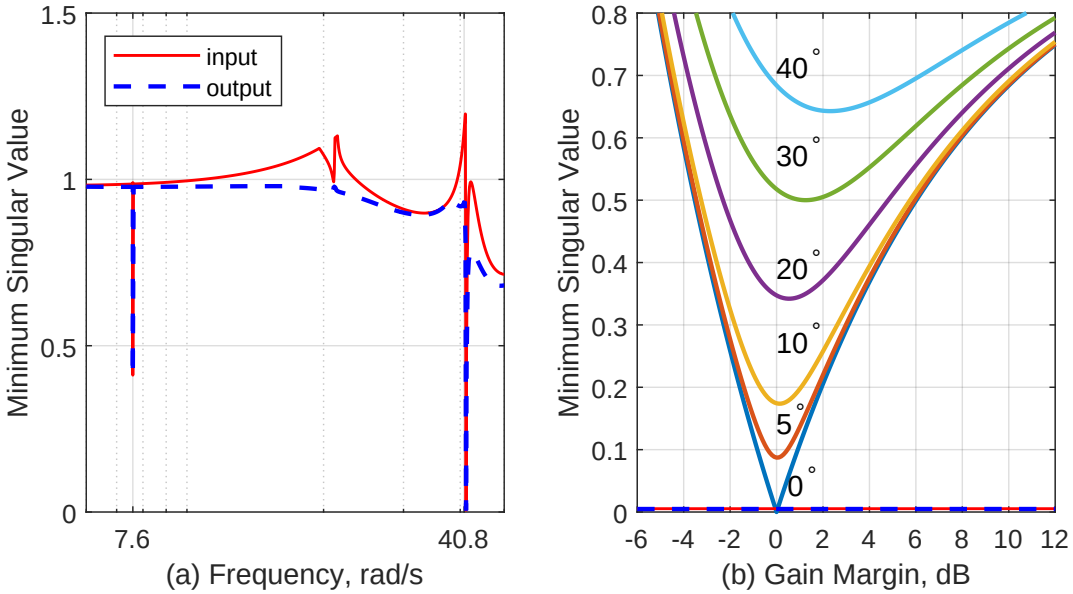


Figure 7.3: The ILAF-controlled system with the 0.8 correction factor at 42 m/s: (a) minimum singular values for the input and output return difference matrices, and (b) the diagram used for universal gain margin and phase margin determination.

### *7.2.1 Gain changes on the aileron inputs*

Figure 6.4 in chapter 6 shows the results of wind-tunnel tests where the gains were varied from 0.6 to 2.0. Figure 7.4, below, shows an attempt to correlate these experimental results with the equivalent conditions on the analytical model. As shown in Fig. 7.4, the closed-loop system is more robust to positive changes in gain than negative changes in gain. The resilience of the physical system is corroborated by the disk margin analyses in Fig. 7.2b.

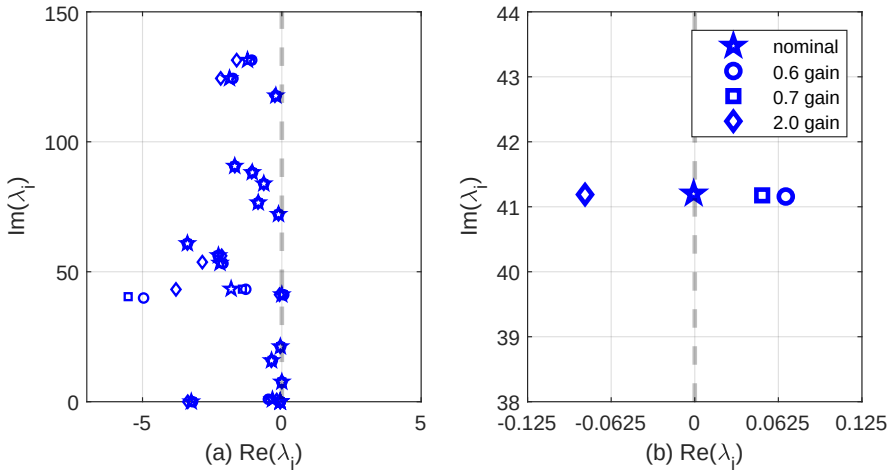


Figure 7.4: (a) Eigenvalues of the ILAF-controlled system at 42 m/s with gain changes on both aileron inputs. (b) Enlarged view showing the poles of the flutter mode.

### *7.2.2 Input Gain and Delay*

Figure 6.6 in chapter 6 shows the results of wind-tunnel tests where a 5 ms delay was applied to both aileron inputs and the gains on the inputs were varied. Figure 7.5 shows that the analytical system remains stable for all perturbations. This observation is consistent with the wind-tunnel results and with the disk margin analysis for the greatly skewed positive eccentricity. As mentioned previously, Fig. 7.2b shows the analytical model to be stable for positive changes in gain and phase.

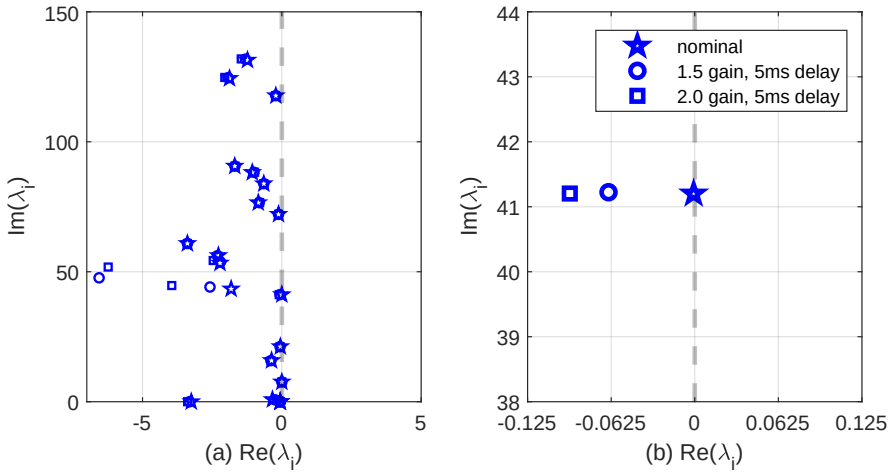


Figure 7.5: (a) Eigenvalues of the perturbed ILAF-controlled system at 42 m/s with gains and delays on both aileron inputs. (b) Enlarged view showing the poles of the flutter mode.

### *7.2.3 Input and Output Perturbations*

Figure 6.7 in chapter 6 shows the result of simultaneous and independent perturbations applied to the inputs and outputs. The input perturbations consisted of a 2 ms delay on both inputs and gains of 1.122 and 0.9, on the right and left ailerons, respectively. Output perturbation 1, labeled $\Delta_1$ in Fig. 7.6, is the addition of a 2 ms delay to all measurement outputs combined with a gain of 1.168, 0.86, 0.86, and 1.168, on the first through fourth outputs. Output perturbation 2, is the same as output perturbation 1 but with the delay increased from 2 ms to 5 ms. Note that these gains were chosen to be tested in the wind tunnel based on the previous robustness analyses of chapter 5. Figure 7.6, below, shows the effects of these perturbations on the closed-loop system. As a reminder, pade approximations were used to add delays to the analytical model. The experimental results, see Fig. 6.7, show the closed-loop ILAF-controlled system to be stable for all perturbations unlike the results shown in Fig. 7.6. Figure 7.6 shows the system to be stable for the input perturbations and the second output perturbation, with the larger delay. However, the system is shown to be unstable for the output perturbation with the smaller delay. There is an obvious discrepancy between the

analytical and physical model. The multivariable stability margins shown in Table 7.3 reflect the fact that the closed-loop system with the aileron correction factor is exceedingly sensitive to the flutter mode at the 42 m/s wind-tunnel speed. This is a consequence of the speed that these analyses were conducted relative to the speed that the analytical model predicts that instability will occur.

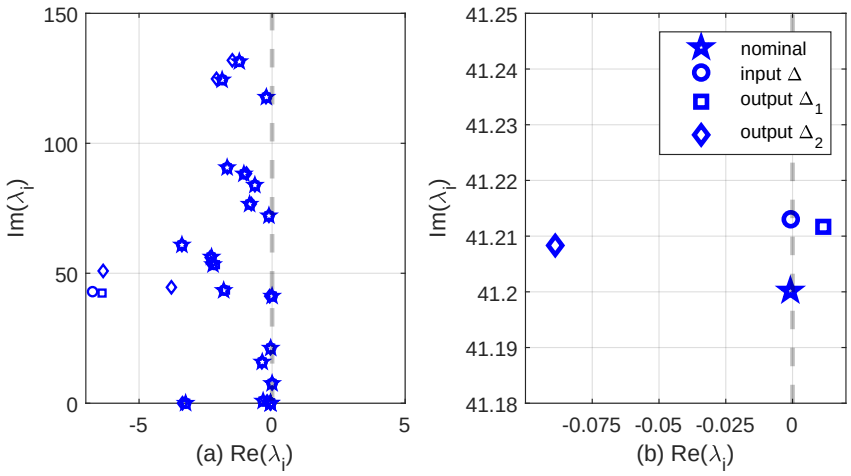


Figure 7.6: (a) Eigenvalues of the ILAF-controlled system for input and output perturbations at 42 m/s. (b) Enlarged view showing the flutter poles associated with the nominal and perturbed systems.

### *7.3 Correlation Analysis - SOF*

In this chapter, the results from the wind-tunnel tests in chapter 6 will be compared against similar tests conducted on the analytical model. The SOF-controlled system was subjected to changes in gain and delays at different wind tunnel speeds; these individual scenarios have been recreated and the results shown with plots of the eigenvalues of the nominal and perturbed system. As discussed previously, third-order Padé approximations were used to incorporate time delays into the closed loop system. The 0.8 correction factor added to the aileron inputs affects both the closed-loop root loci, and the robustness analyses performed previously. In order to facilitate correlations between analysis and experimentation, the closed-loop root loci and robustness tests for the model

including the 0.8 correction factor are shown concisely below. For brevity, the discussion of the robustness tests will be omitted. The reader is referred to chapters 3 and 5 for more info on the multivariable stability margins. Note that, since the predicted closed-loop flutter speed is less than 50 m/s, correlations at a wind-tunnel speed of 50 m/s between the analytical model and the robustness measures, and the experimental results cannot be performed. The closed-loop locus for wind-tunnel speeds from 15 m/s to 60 m/s is shown in Fig. 7.7, and the robustness analyses are shown in Figs. 7.8 and 7.9.

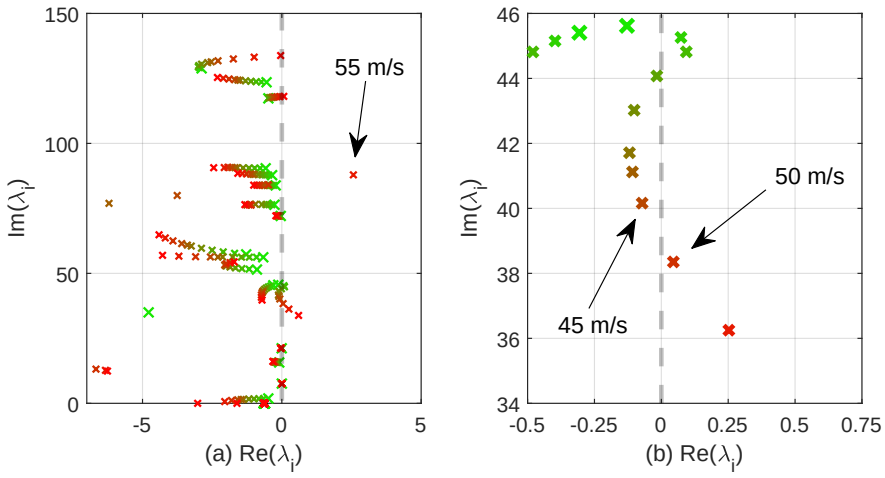


Figure 7.7: (a) SOF-controlled closed-loop root locus for the updated model with 0.8 correction factor for air-speeds from 15 m/s (green) to 60 m/s (red). (b) Enlarged view showing the closed-loop flutter speed close to 49 m/s.

Figure 7.7 shows the closed-loop flutter speed to be approximately 49 m/s. The results shown in Fig. 7.7 underestimate the results seen in Fig. 6.8, where the closed-loop system was seen to be stable at 50 m/s in the wind-tunnel. The stability summary shown in Table 7.4, shows similar margins at the inputs and outputs using both the DM and UGM methods.

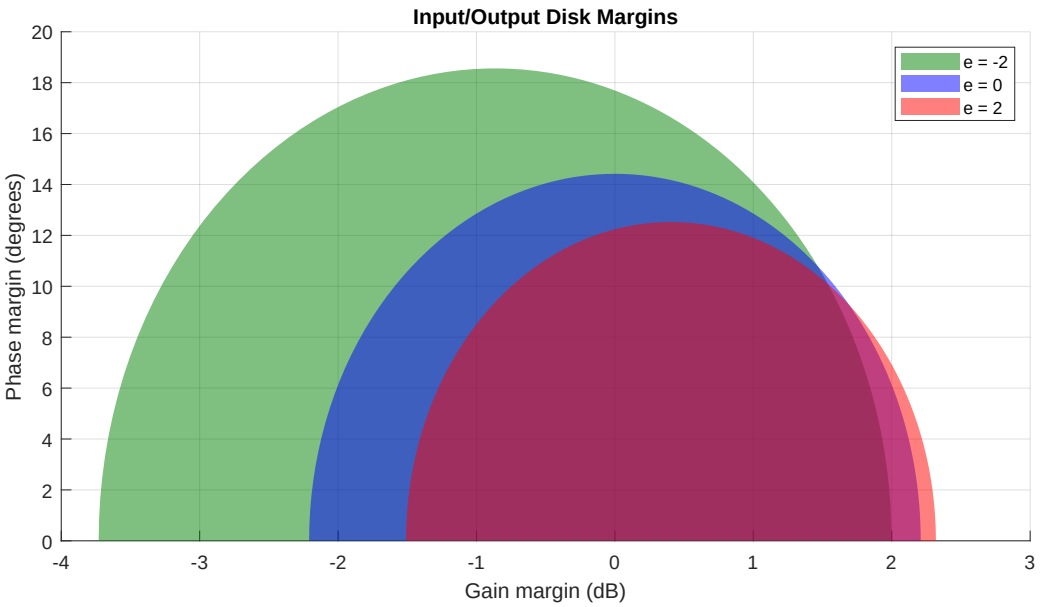


Figure 7.8: Input/output disk margins for three different eccentricities for the analytical model with the 0.8 correction factor on the aileron inputs operated at a wind-tunnel speed of 42 m/s.

| | | DM | UGM |
|---|---|---|---|
| Input | Gain Margin, dB | $[-2.21, 2.21]$ | $[-1.82, 2.31]$ |
| | Phase Margin, ° | 14.42 | 13.40 |
| Output | Gain Margin, dB | $[-2.21, 2.21]$ | $[-1.72, 2.14]$ |
| | Phase Margin, ° | 14.42 | 12.54 |

Table 7.4: Stability margin summary for the SOF controller with the 0.8 correction factor added to the aileron inputs at a wind-tunnel speed of 42 m/s.

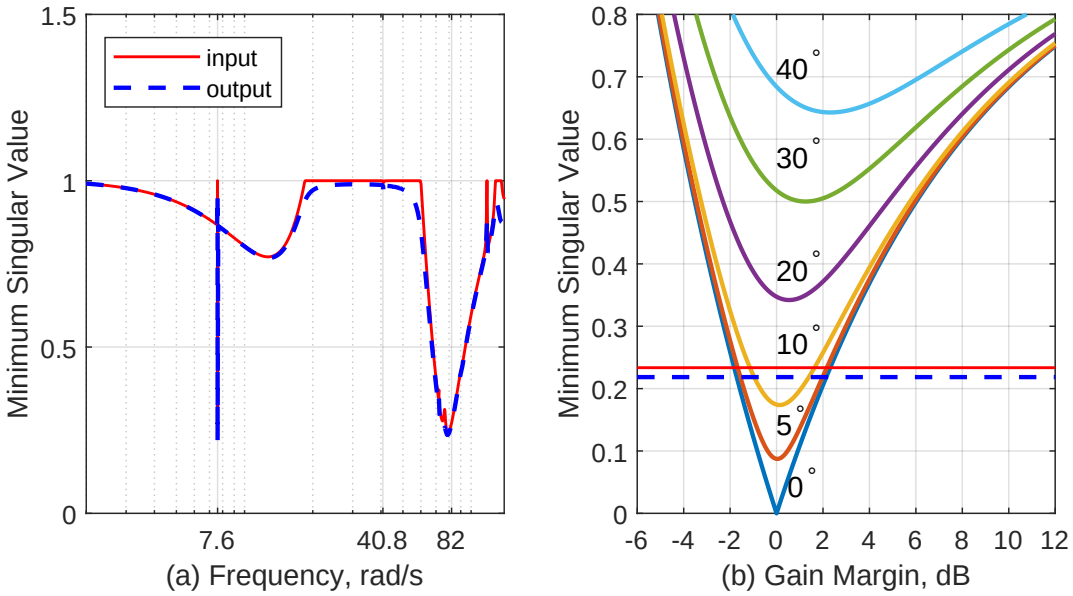


Figure 7.9: The SOF-controlled system with the 0.8 correction factor at 42 m/s: (a) minimum singular values for the input and output return difference matrices; (b) the diagram used for universal gain margin and phase margin determination.

### *7.3.1 Gain changes to the aileron inputs at a wind-tunnel speed of 41.5 m/s*

The perturbed root locus shown in Fig. 7.10 is related to the results shown in Fig. 6.9 of chapter 6. The closed-loop SOF-controlled system was shown stable in Fig. 6.9 for the nominal condition and for gains of 0.4 and 0.2. The stability for these gains is shown on the perturbed root locus in Fig. 7.12. Though not shown, a gain of 1.5 on both aileron inputs would make the analytical model unstable at 42 m/s. There is some correlation between these ideas, as the physical hardware and the analytical model both seem more resilient to decreases in gain rather than increases in gain. The apparent robustness to decreases in gain can also be seen in the disk margin analysis of Fig. 7.8.

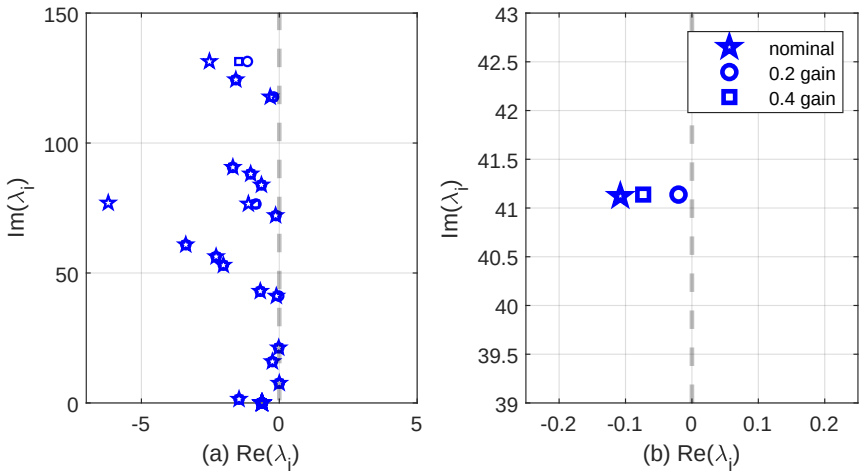


Figure 7.10: (a) Eigenvalues of the SOF-controlled system with the 0.8 correction factor for gains on the aileron inputs at a wind-tunnel speed of 42 m/s. (b) Enlarged view showing the eigenvalues of the nominal and perturbed systems associated with the 40 rad/s flutter mode.

### *7.3.2 Gain changes to the aileron inputs at a wind-tunnel speed of 45 m/s*

The closed-loop root locus of the nominal and perturbed system shown in Fig. 7.11 corresponds to the experimental results seen in Fig. 6.10. Figure 6.10 shows the SOF-controlled system to be

stable at a wind-tunnel speed of 46 m/s for gains of 0.4 and 0.6 applied to the aileron inputs. The perturbed eigenvalues of Fig. 7.11 show the analytical model to be unstable at a gain of 0.4. Though not shown here, for brevity, similar analyses to Fig. 5.10 and Fig. 5.9 reveal the SOF-controlled system with the 0.8 correction factor to have a multi-loop gain margin, at 45 m/s, of approximately 1.5 dB. As a result, the wind-tunnel test results shown in Fig. 4.3 indicate considerably more robustness to decreases in gain than are shown in the analyses of the analytical model. Once again, the discrepancy does not indicate that the multi-loop methods are conservative, as the eigenvalues clearly show instability, but likely an indication of model inaccuracy.

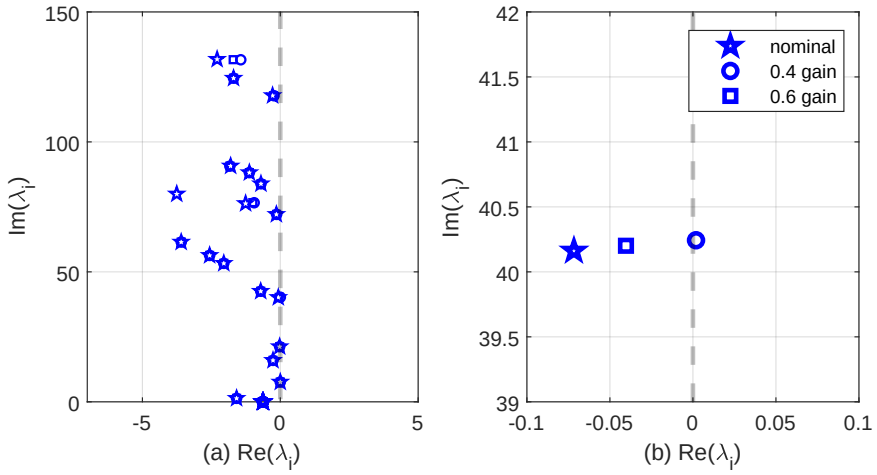


Figure 7.11: (a) Eigenvalues of the SOF-controlled system with the 0.8 correction factor for gains on the aileron inputs at a wind-tunnel speed of 45 m/s. (b) Enlarged view showing the eigenvalues of the nominal and perturbed systems associated with the 40 rad/s flutter mode.

### *7.3.3 Delays added to the aileron inputs at a wind-tunnel speed of 41.5 m/s*

The results shown in Fig. 6.12, of chapter 6, are recreated in Fig. 7.12, below. The experimental results in Fig. 6.12 show the system to be stable with a delay of 3 ms, and unstable for a delay of 5 ms. For context, a 3 ms and 5 ms delay at the frequency of peak sensitivity, seen in Fig. 7.9a,

correspond to a phase change of 13 and 23 degrees, respectively. The stability margin summary in Table 7.4 shows the analytical model for the SOF-controlled system to be robust to the 3 ms delay. However, the physical model was destabilized by the 5 ms delay. As the eigenvalues shown in Fig. 7.12b are clearly stable while the response in Fig. 6.12c is not stable, the likely culprit is a mismatch between the analytical and physical model.

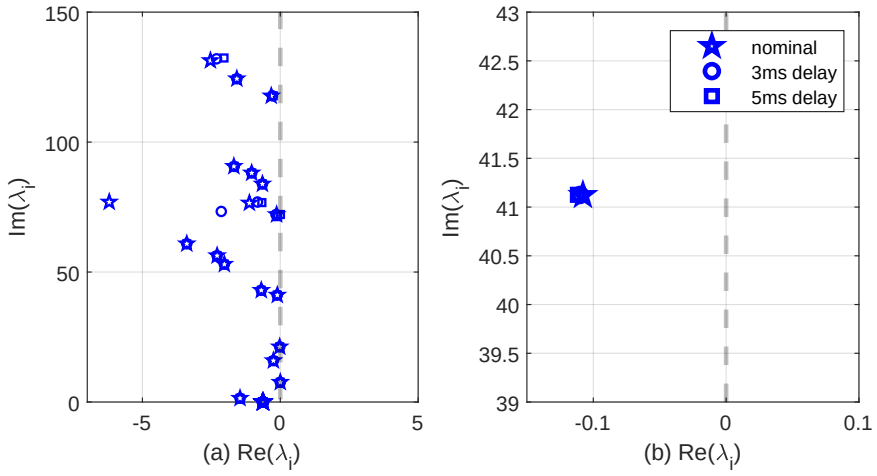


Figure 7.12: (a) Eigenvalues of the SOF-controlled system with the 0.8 correction factor for delays added to the aileron inputs at a wind-tunnel speed of 41.5 m/s. (b) Enlarged view showing the eigenvalues of the nominal and perturbed systems associated with the 40 rad/s flutter mode.

## *7.4 Correlation Analysis - LQG*

In this chapter, a correlation of analysis and experiment is conducted for the LQG-controlled system. The experimental results are those of chapter 6, while the analyses are concisely recreated below for the analytical model with the 0.8 correction factor applied to the aileron inputs. These analyses include a new closed-loop root locus, along with disk margin and universal gain margin analyses across the various speeds experienced by the LQG-controlled system in the wind tunnel. The updated closed-loop root locus can be seen in Fig. 7.13, and the updated stability-margin analyses can be seen in Fig. 7.14 - 7.17. The ultimate flutter speed of the LQG-controlled system

was seen in the wind tunnel, see Fig. 6.13, to be 46.5 m/s, while the closed-loop root locus in Fig. 7.13 shows the ultimate flutter speed to be approximately 48 m/s to 49 m/s – roughly a 4.5 percent difference. It is worth pointing out that, as the results shown in Fig. 6.13 were created with a gain of 1.2 on the aileron inputs, and the results in Fig. 7.13 have also used a gain of 1.2 on the aileron inputs. The multi-loop margins shown in Figs. 7.14 - 7.17 and Table 7.5 show good robust margins at the aileron inputs but poor robustness at the measurement outputs.

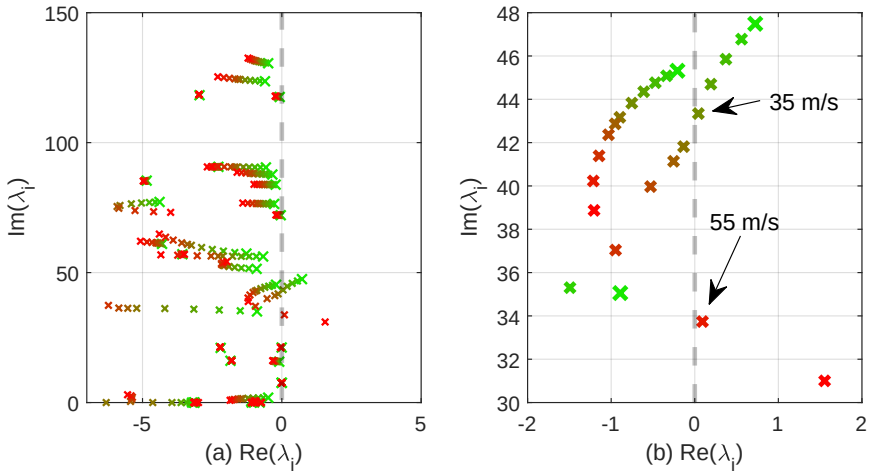


Figure 7.13: (a) LQG-controlled closed-loop root locus for the updated model with 0.8 correction factor for air-speeds from 15 m/s (green) to 60 m/s (red). (b) Enlarged view showing the closed-loop flutter speed close to 42 m/s.

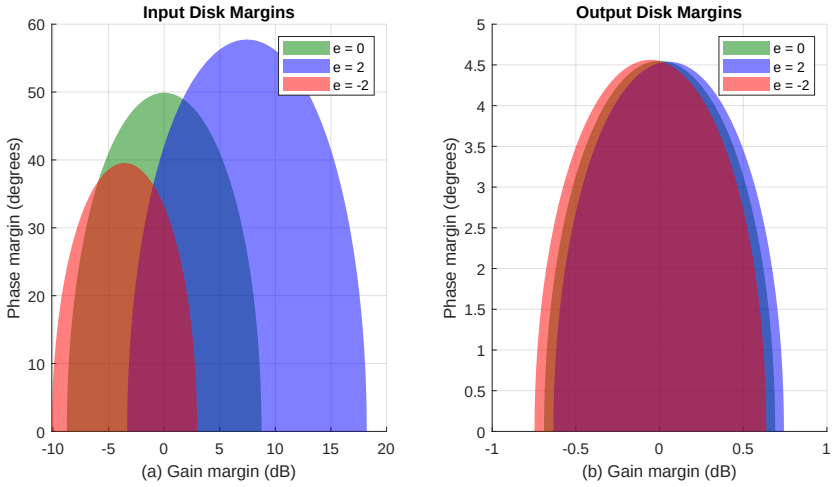


Figure 7.14: Input disk margins for the LQG-controlled system with the 0.8 correction factor: (a) balanced disk margin; (b) disk margin heavily-skewed towards positive changes in gain.

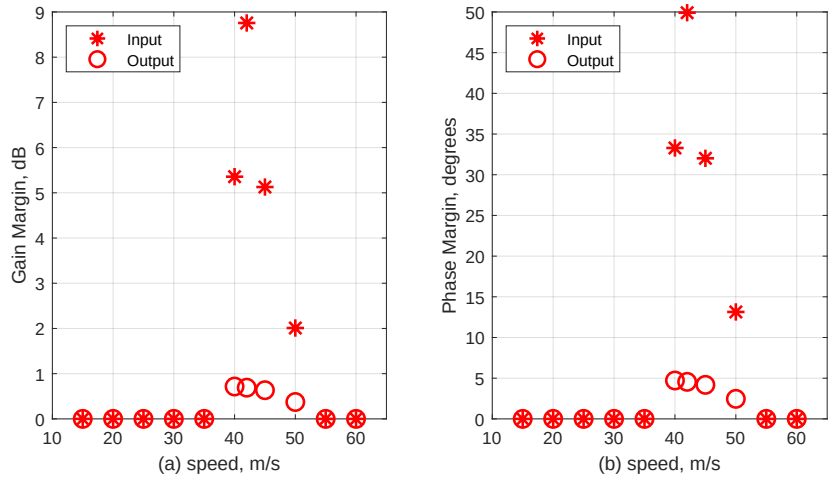


Figure 7.15: Balanced disk margins for the LQG-controlled system with the 0.8 correction factor for speeds from 15 m/s to 60 m/s: (a) Gain Margin, (b) Phase Margin.

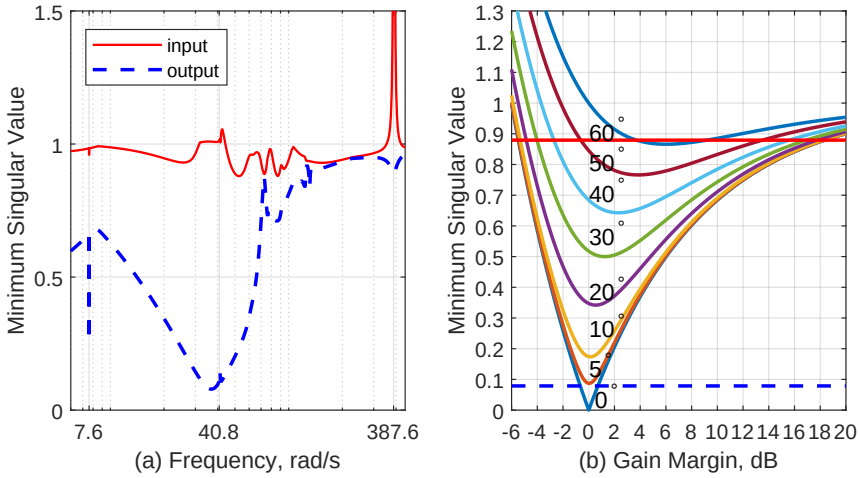


Figure 7.16: The LQG-controlled system with the 0.8 correction factor at 42 m/s: (a) minimum singular values for the input and output return difference matrices; (b) The diagram used for universal gain margin and phase margin determination.

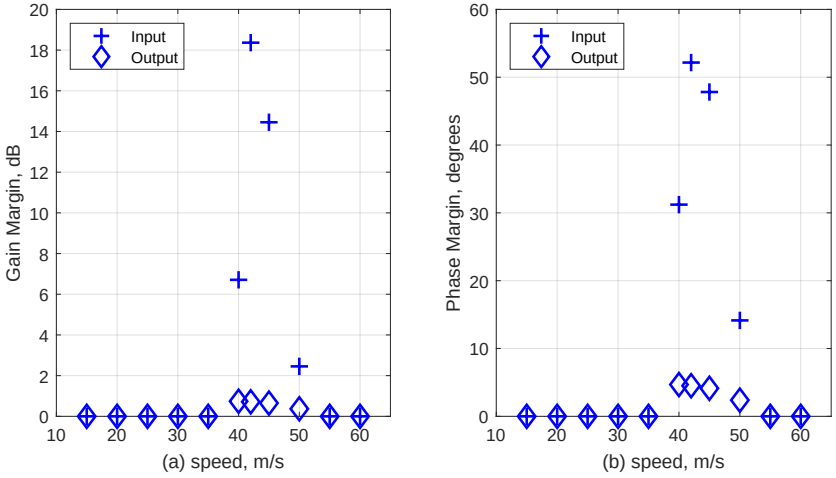


Figure 7.17: Universal Gain and Phase Margins for the LQG-controlled system with the 0.8 correction factor for speeds from 15 m/s to 60 m/s: (a) Gain Margin, (b) Phase Margin.

| | | DM | UGM |
|---|---|---|---|
| Input | Gain Margin, dB | $[-8.76, 8.76]$ | $[-5.48, 18.36]$ |
| | Phase Margin, $^\circ$ | 49.91 | 52.16 |
| Output | Gain Margin, dB | $[-0.70, 0.70]$ | $[-0.66, 0.71]$ |
| | Phase Margin, $^\circ$ | 4.55 | 4.50 |

Table 7.5: Stability margin summary for the LQG controller with the 0.8 correction factor added to the aileron inputs at the open-loop flutter speed of 41.5 m/s.

### *7.4.1 Gain changes on the aileron inputs at the open-loop flutter speed*

The analytical results shown in Fig. 7.18 are in agreement with the experimental results shown in Fig. 6.14 from chapter 6. The multi-loop margins shown in Table 7.5 are also in agreement with this conclusion as these margins are quite large and the perturbations on the aileron inputs, 0.9 and 1.2, were quite small.

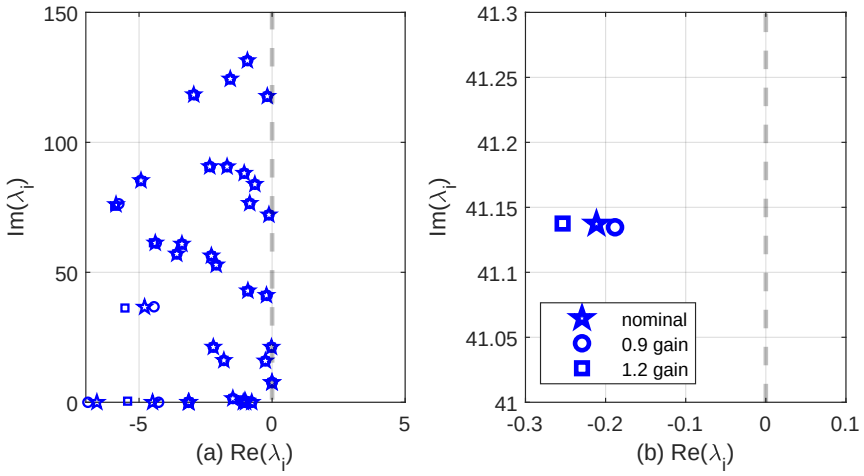


Figure 7.18: (a) Eigenvalues of the LQG-controlled system with the 0.8 correction factor for gains added to the aileron inputs. (b): Enlarged view showing the eigenvalues of the nominal and perturbed systems associated with the 40 rad/s flutter mode.

### *7.4.2 Delays added to the aileron inputs at the open-loop flutter speed*

Figure 7.19, below, shows the recreation on the analytical model of the wind-tunnel test results shown in Fig. 6.15. The analytical and experimental test results are in alignment, as the qualitative response shown in Fig. 6.15 is stable and there are no poles in the RHP in Fig. 7.19. The stability analyses, Table 7.5, also agree with these results.

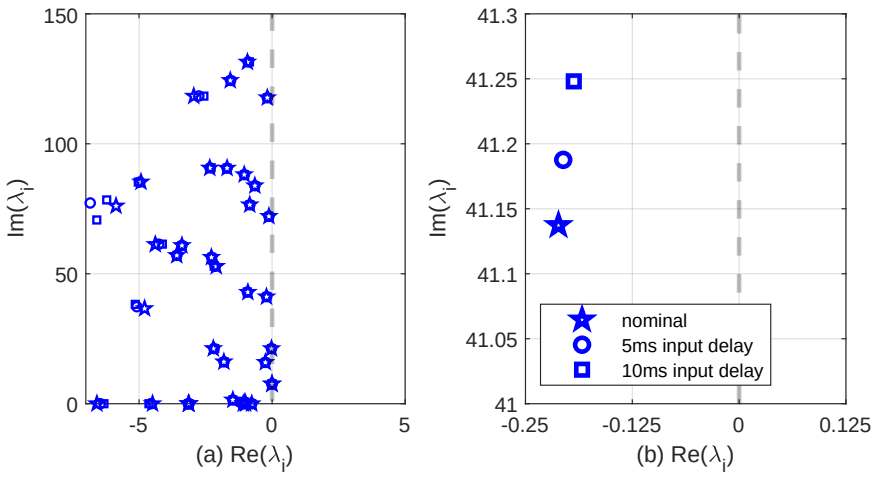


Figure 7.19: (a) Eigenvalues of the LQG-controlled system with the 0.8 correction factor for delays added to the aileron inputs. (b) Enlarged view showing the eigenvalues of the nominal and perturbed systems associated with the 40 rad/s flutter mode.

### *7.4.3 Delays added to the aileron inputs across several wind-tunnel speeds*

The wind-tunnel test results shown in Fig. 6.16 are recreated in the plot of the nominal and perturbed eigenvalues for wind-tunnel speeds from 40 m/s to 45 m/s shown in Fig. 7.20. The eigenvalues shown in Fig. 7.20b correspond to wind-tunnel speeds of 40 m/s, 42 m/s, and 45 m/s, from the upper right to lower left, respectively. As expected based on the stability margin analyses in Fig. 7.15, and Fig. 7.17, the analytical model is quite robust to changes in phase. Near the destabilizing test condition shown in Fig. 6.16, the analytical model should have greater than $30^\circ$ of multi-loop phase margin, which would correspond to a delay on both aileron inputs of approximately 13 ms. Consequently, there appears to be a difference in multi-loop phase margin between the analytical model at 45 m/s and the physical hardware at 44.5 m/s of approximately $18^\circ$.

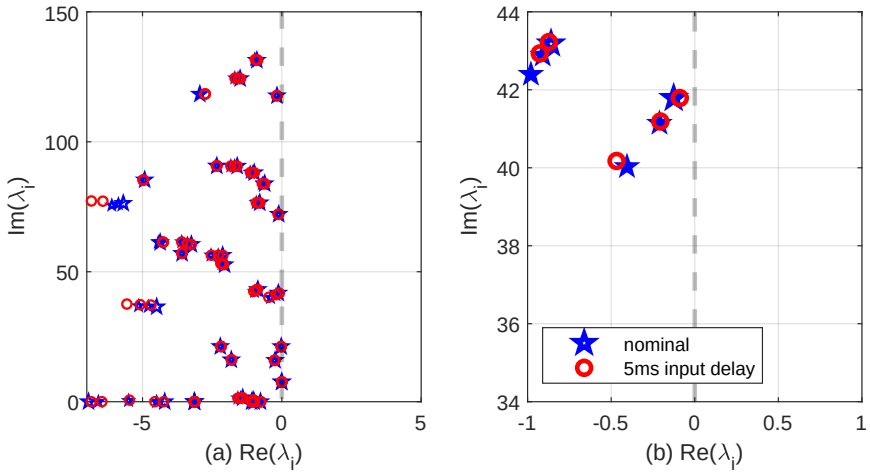


Figure 7.20: (a) Eigenvalues of the LQG-controlled system with the 0.8 correction factor for delays added to the aileron inputs at wind-tunnel speeds of 40 m/s, 42 m/s, and 45 m/s. (b) Enlarged view showing the eigenvalues of the nominal and perturbed systems associated with the 40 rad/s flutter mode for three different wind-tunnel speeds.

## *7.5 Discussion of Experimental and Analytical Correlation Results*

The development of aeroservoelastic math models during the design evolution of an airplane or a wind tunnel model is a gradual process in which best mathematical / numerical tools are used first to create a first math model with which control law development can begin. This is followed by a gradual process of math model improvement as more test data and results from high-fidelity simulations become available and as the configuration reaches maturity. New control laws are developed periodically throughout the process.

Knowing that system math models are uncertain, with more uncertainty early in the development process and less uncertainty later, closed-loop robustness analysis can be used (in addition to the necessary stability and performance analyses) in two ways. First, at the early stages of the design and development process, control law synthesis may require large robustness margins in anticipation of the model changes that would come. Once the final configuration has been frozen, and

with as much high-fidelity analysis and test information as possible and practical to support ”best possible” math models, control robustness measures must be demonstrated to protect the system against that level of uncertainty and those probable variations that may still be encountered in real life.

The analysis, synthesis, and test program demonstrate all this. Beginning with a ”best practice” math model that was created early in the wind tunnel model development process, preliminary control laws were synthesized and their robustness levels, based on the original math model of the system were checked. Tests using these control laws were carried out next and were used to improve the math model of the system (the aileron aerodynamic effectiveness correction) and to vary the properties of the system in order to study how well the control laws performed. Not surprisingly, control laws that were created based on a math model that missed certain aspects of system behavior were found to be less robust to changes in the system when studied with the improved math model of the system. In the design process of an actively controlled airplane new control laws would be synthesized now based on the most up to date math model, subject to certification robustness constraints that would protect the system against uncertainties that the best math models (given state of the art analysis and testing practices) may not capture.

# Chapter 8

# CONCLUSION

Control law synthesis for active flutter suppression followed the design and development of an active flexible wind tunnel model representative of high aspect ratio commercial aircraft. An initial ”best practice” math model of the structural dynamics, unsteady aerodynamics, sensing, and actuation of the system was used to synthesize three control laws that would stabilize the system against flutter over a range of speeds below and above the passive open-loop flutter speed. Three methods for establishing closed-loop robustness measures were used to quantify the robustness of the system based on its initial mathematical model. The system was then tested with these control laws and their robustness to system variations in the wind tunnel was studied. Such variations, in tests, included speed variations as well as gain and phase variations in the control loops, representing gain and phase uncertainties in the system. This was followed by revisiting the robustness of the control laws tested mathematically, this time with a more accurate mathematical model of the system.

The work highlights the importance of (a) working with as high accuracy math models of the system as possible, (b) understanding the key sources and types of uncertainties possible, (c) evolving the control laws during the vehicle development process to account for initial uncertainties in the models that can be large and then ending with final control laws that demonstrate sufficient robustness (as required by certification agencies) with the most accurate math models available and then tested in flight at selected critical conditions subject to selected variations in the system.

The work adds insight regarding the kind of model variations that the control designer needs to consider and the way different measures of system robustness compare to one another and relate to the capacity of the control design to address model uncertainties.

Other robust control techniques may be used. The more test results in the wind tunnel and

in flight will be available the more firm the basis will be on which the safety of active flutter suppression technology will be assessed and accepted for application.

It would be nice to go back to the wind tunnel with the model and the capabilities described here to test new control laws that would be developed based on a much improved math model of the system. With such a mature and accurate math model, control laws should be synthesized to meet constraints on their level of robustness in the flight envelope and its safety margins that would resemble what may become required robustness of active control systems in the aircraft industry.

# BIBLIOGRAPHY

[1] Livne, E., "Aircraft Active Flutter Suppression: State of the Art and Technology Maturation Needs," *Journal of Aircraft*, Vol. 55, No. 1, 2018, pp. 410–452. https://doi.org/10.2514/1.C034442.

[2] Burnett, E. L., Beranek, J. A., Holm-Hansen, B. T., Atkinson, C. J., and Flick, P. M., "Design and flight test of active flutter suppression on the X-56A multi-utility technology test-bed aircraft," *The Aeronautical Journal*, Vol. 120, No. 1228, 2016, pp. 893–909. https://doi.org/10.1017/aer.2016.41.

[3] Schmidt, D. K., "Stability Augmentation and Active Flutter Suppression of a Flexible Flying-Wing Drone," *Journal of Guidance, Control, and Dynamics*, Vol. 39, No. 3, 2016, pp. 409–422. https://doi.org/10.2514/1.G001484.

[4] Schmidt, D. K., Danowsky, B. P., Kotikalpudi, A., Theis, J., Regan, C. D., Seiler, P. J., and Kapania, R. K., "Modeling, Design, and Flight Testing of Three Flutter Controllers for a Flying-Wing Drone," *Journal of Aircraft*, 2020, pp. 1–19. https://doi.org/10.2514/1.C035720.

[5] Theis, J., Pfifer, H., and Seiler, P., "Robust Modal Damping Control for Active Flutter Suppression," *Journal of Guidance, Control, and Dynamics*, Vol. 43, No. 6, 2020, pp. 1056–1068. https://doi.org/10.2514/1.G004846.

[6] Takarics, B., Patartics, B., Luspay, T., Vanek, B., Roessler, C., Bartasevicius, J., Koeberle, S. J., Hornung, M., Teubl, D., Pusch, M., Wustenhagen, M., Kier, T. M., Looye, G., Bauer, P., Meddaikar, Y. M., Waitman, S., and Marcos, A., "Active Flutter Mitigation Testing on the FLEXOP Demonstrator Aircraft," *AIAA Scitech 2020 Forum*, 2020. https://doi.org/10.2514/6.2020-1970, AIAA Paper 2020-1970.

[7] Lehtomaki, N., Sandell, N., and Athans, M., "Robustness Results in Linear-Quadratic Gaussian Based Multivariable Control Designs," *IEEE Transactions on Automatic Control*, Vol. 26, No. 1, 1981, pp. 75–93. https://doi.org/10.1109/TAC.1981.1102565.

[8] Sidi, M. J., *Design of Robust Control Systems, From Classical to Modern Practical Approaches*, Krieger Pub Co, 2001.

[9] Yedavalli, R. K., *Robust Control of Uncertain Dynamic Systems*, Springer New York, New York, NY, 2014. https://doi.org/10.1007/978-1-4614-9132-3.

[10] Mukhopadhyay, V., and Newsom, J. R., "A multiloop system stability margin study using matrix singular values," *Journal of Guidance, Control, and Dynamics*, Vol. 7, No. 5, 1984, pp. 582–587. https://doi.org/10.2514/3.19898.

[11] Newsom, J. R., and Mukhopadhyay, V., "A multiloop robust controller design study using singular value gradients," *Journal of Guidance, Control, and Dynamics*, Vol. 8, No. 4, 1985, pp. 514–519. https://doi.org/10.2514/3.20013.

[12] Marchetti, L., De Gaspari, A., Riccobene, L., Toffol, F., Fonte, F., Ricci, S., Mantegazza, P., Livne, E., and Hinson, K. A., "Active Flutter Suppression Analysis and Wind Tunnel Studies of an Uncertain Commercial Transport Configuration," *AIAA Scitech 2020 Forum*, American Institute of Aeronautics and Astronautics, Reston, Virginia, 2020. https://doi.org/10.2514/6.2020-1677, AIAA Paper 2020-1677.

[13] Ricci, S., Marchetti, L., Riccobene, L., De Gaspari, A., Toffol, F., Fonte, F., Mantegazza, P., Berg, J., Morgansen, K., and Livne, E., "An Active Flutter Suppression (AFS) Project: Overview, Results and Lessons Learned," *AIAA SciTech Conference*, 2021. AIAA Paper 2021-0908.

[14] Wykes, J. H., and Mori, A. S., "Techniques and Results of an Analytical Investigation into Controlling the Structural Modes of Flexible Aircraft," *Symposium on Structural Dynamics and Aeroelasticity*, American Institute of Aeronautics and Astronautics, Reston, Virigina, 1965. https://doi.org/10.2514/6.1965-1140, AIAA Paper 1965-1140.

[15] Wykes, J., and Knight, R., "Progress report on a gust alleviation and structural dynamic stability augmentation system (GASDSAS) design study," *3rd Annual Meeting*, American Institute of Aeronautics and Astronautics, Reston, Virigina, 1966. https://doi.org/10.2514/6.1966-999, AIAA Paper 1966-999.

[16] Wykes, J. H., "Structural dynamic stability augmentation and gust alleviation of flexible aircraft," *5th Annual Meeting and Technical Display*, American Institute of Aeronautics and Astronautics, Reston, Virigina, 1968. https://doi.org/10.2514/6.1968-1067, AIAA Paper 1968-1067.

[17] Wykes, J. H., Klepl, M. J., and Brosnan, M. J., "Flight Test and Analyses of the B-1 Structural Mode Control System at Supersonic Flight Conditions," Tech. rep., NASA, 1983. NASA-CR-170405.

[18] Ghiringhelli, G. L., Lanz, M., and Mantegazza, P., "Active flutter suppression for a wing model," *Journal of Aircraft*, Vol. 27, No. 4, 1990, pp. 334–341. https://doi.org/10.2514/3.25277.

[19] Ghiringhelli, G. L., Lanz, M., Mantegazza, P., and Ricci, S., "Active Flutter Suppression Techniques in Aircraft Wings," *Control and Dynamic Systems*, Vol. 92, 1992, pp. 57–115. https://doi.org/10.1016/B978-0-12-012752-8.50007-6.

[20] Fonte, F., Ricci, S., and Mantegazza, P., "Gust Load Alleviation for a Regional Aircraft Through a Static Output Feedback," *Journal of Aircraft*, Vol. 52, No. 5, 2015, pp. 1559–1574. https://doi.org/10.2514/1.C032995.

[21] R. PELOUBET, J., "YF16 active-control-system/structural dynamics interaction instability," *16th Structural Dynamics, and Materials Conference*, 1975. https://doi.org/10.2514/6.1975-823, URL https://arc.aiaa.org/doi/abs/10.2514/6.1975-823, AIAA Paper 1975-823.

[22] Silva, R., Mello, O., Azevedo, J., Chen, P., and Liu, D., "Investigation on Transonic Correction Methods for Unsteady Aerodynamics and Aeroelastic Analyses," *Journal of Aircraft*, Vol. 45, No. 6, 2008, pp. 1890–1903. https://doi.org/10.2514/1.33406.

[23] Wu, S., and Livne, E., "Probabilistic Aeroservoelastic Reliability Assessment Considering Control System Component Uncertainty," *AIAA Journal*, Vol. 54, 2016, pp. 2507–2520. https://doi.org/10.2514/1.J054824.

[24] Wu, S., and Livne, E., "Alternative Aerodynamic Uncertainty Modeling Approaches for Flutter Reliability Analysis," *AIAA Journal*, Vol. 55, 2017, pp. 2808–2823. https://doi.org/10.2514/1.J055334.

[25] Doyle, J. C., "Robustness of multiloop linear feedback systems," *1978 IEEE Conference on Decision and Control including the 17th Symposium on Adaptive Processes*, 1978, pp. 12–18. https://doi.org/10.1109/CDC.1978.267885.

[26] Doyle, J., "Analysis of Feedback Systems With Structured Uncertainties." *IEE Proceedings D: Control Theory and Applications*, Vol. 129, No. 6, 1982, pp. 242–250. https://doi.org/10.1049/ip-d.1982.0053.

[27] Blight, J. D., Lane Dailey, R., and Gangsaas, D., "Practical control law design for aircraft using multivariable techniques," *International Journal of Control*, Vol. 59, No. 1, 1994, pp. 93–137. https://doi.org/10.1080/00207179408923071.

[28] Seiler, P., Packard, A., and Gahinet, P., "An Introduction to Disk Margins [Lecture Notes]," *IEEE Control Systems Magazine*, Vol. 40, No. 5, 2020, pp. 78–95. https://doi.org/10.1109/MCS.2020.3005277.

[29] Syrmos, V., Abdallah, C., Dorato, P., and Grigoriadis, K., "Static output feedback—A survey," *Automatica*, Vol. 33, No. 2, 1997, pp. 125–137. https://doi.org/10.1016/S0005-1098(96)00141-0.

[30] Skogestad, S., and Postlethwaite, I., *Multivariable feedback control: analysis and design*, 2nd ed., Wiley-Interscience, 2005.

[31] Levine, W., and Athans, M., "On the determination of the optimal constant output feedback gains for linear multivariable systems," *IEEE Transactions on Automatic Control*, Vol. 15, No. 1, 1970, pp. 44–48. https://doi.org/10.1109/TAC.1970.1099363.

[32] Anderson, B. D., and Moore, J. B., *Optimal Control, Linear Quadratic Methods*, Prentice-Hall, 1990.

[33] Broussard, J. R., and Halyo, N., "Active flutter control using discrete optimal constrained dynamic compensators," *1983 American Control Conference*, IEEE, 1983, pp. 1026–1034. https://doi.org/10.23919/ACC.1983.4788265.

[34] Kwakernaak, H., and Sivan, R., *Linear Optimal Control Systems*, Wiley-interscience New York, 1972.

[35] Losser, Y., "Ajustement de lois de commande application en aéronautique," Ph.D. Thesis, École nationale supérieure de l'aéronautique et de l'espace, Toulouse, 2006.

[36] Patil, M. J., and Hodges, D. H., "Output Feedback Control of the Nonlinear Aeroelastic Response of a Slender Wing," *Journal of Guidance, Control, and Dynamics*, Vol. 25, No. 2, 2002, pp. 302–308. https://doi.org/10.2514/2.4882.

[37] Miyazawa, Y., and Dowell, E., "Robust control system design with multiple model approach and its application to active flutter control," *Guidance, Navigation and Control Conference*, American Institute of Aeronautics and Astronautics, Reston, Virigina, 1989, pp. 1989–3578. https://doi.org/10.2514/6.1989-3578, AIAA Paper 1989-3578.

[38] Moerder, D., and Calise, A., "Convergence of a numerical algorithm for calculating optimal output feedback gains," *IEEE Transactions on Automatic Control*, Vol. 30, No. 9, 1985, pp. 900–903. https://doi.org/10.1109/TAC.1985.1104073.

[39] Bingulac, S., Cuk, N., and Calovic, M., "Calculation of optimum feedback gains for output-constrained regulators," *IEEE Transactions on Automatic Control*, Vol. 20, No. 1, 1975, pp. 164–166. https://doi.org/10.1109/TAC.1975.1100863.

[40] Collins, E., Haddad, W., and Ying, S., "Reduced-order dynamic compensation using the Hyland-Bernstein optimal projection equations," *Proceedings of 1995 American Control Conference - ACC'95*, Vol. 1, American Autom Control Council, 1995, pp. 539–543. https://doi.org/10.1109/ACC.1995.529307.

[41] Dardel, M., and Bakhtiari-Nejad, F., "Limit cycle oscillation control of wing with static output feedback control method," *Aerospace Science and Technology*, Vol. 24, No. 1, 2013, pp. 147–160. https://doi.org/10.1016/j.ast.2011.08.013.

[42] Toivonen, H. T., and Mäkilä, P. M., "Newton's method for solving parametric linear quadratic control problems," *International Journal of Control*, Vol. 46, No. 3, 1987, pp. 897–911. https://doi.org/10.1080/00207178708547402.

[43] Rautert, T., and Sachs, E. W., "Computational Design of Optimal Output Feedback Controllers," *SIAM Journal on Optimization*, Vol. 7, No. 3, 1997, pp. 837–852. https://doi.org/10.1137/S1052623495290441.

[44] Gangsaas, D., and Ly, U.-L., "APPLICATION OF A MODIFIED LINEAR QUADRATIC GAUSSIAN DESIGN TO ACTIVE CONTROL OF A TRANSPORT AIRPLANE," *Guidance and Control Conference*, American Institute of Aeronautics and Astronautics, 1979. https://doi.org/10.2514/6.1979-1746.

[45] Gangsaas, D., Ly, U., and Norman, D. C., "Practical Gust Load Alleviation and Flutter Suppression Control Laws Based on a LQG Methodology," *AIAA Paper*, 1981. https://doi.org/10.2514/6.1981-21.

[46] Doyle, J. C., and Stein, G., "Robustness with observers," *1978 IEEE Conference on Decision and Control including the 17th Symposium on Adaptive Processes*, 1978, pp. 1–6. https://doi.org/10.1109/CDC.1978.267883.

[47] Simon, D., *Additional topics in Kalman filtering*, chapter and pages, pp. 297–329. https://doi.org/10.1002/0470045345.ch10.

[48] Riebe, J., "A Correlation of Two-Dimensional Data on Lift Coefficient Available With Blowing-, Suction-, Slotted-, And Plain-Flap High-Lift Devices," *NACA RM L55D29a*, 1955.